Three-dimensional wake transition of a diamond-shaped cylinder

Hongyi Jiang[1†]
[1]School of Engineering, The University of Western Australia, 35 Stirling Highway, Perth, WA 6009, Australia

Abstract

Three-dimensional (3D) wake transition for flow past a diamond cylinder is investigated numerically. Detailed 3D direct numerical simulations (DNS) show that the wake is represented by mode A with global vortex dislocations for Reynolds numbers Re = 121 – 150, followed by a mode swapping between modes A and B for Re = 160 – 210 and increasingly disordered mode B for $Re \geq 220$. In the mode swapping regime, different characteristics of the dislocation and non-dislocation periods are revealed by decomposing flow properties (e.g. the root-mean-square lift coefficient) into the values corresponding to the dislocation and non-dislocation periods. Such decomposition helps to explain some major differences observed for the cases of a diamond and a circular cylinder. In addition to DNS, Floquet stability analyses are conducted to identify the 3D wake instability modes of a diamond cylinder up to Re = 300. Phase-averaged base flow is used to eliminate the quantitative uncertainties induced by the aperiodic secondary vortex street of the base flow. Interestingly, a subharmonic instability mode is identified at $Re \geq 285$, whereas mode B is absent. The origin of the subharmonic mode is explained. The disagreement between the DNS and the Floquet analysis regarding the existence of mode B and the subharmonic mode is also explained. It is found that the natural 3D flow involves complex interactions between the streamwise and spanwise vortices, as well as between the 3D wake transition and the two-dimensional base-flow transition, which excite mode B and suppress the subharmonic mode.

1. Introduction

Steady incoming flow past a smooth and nominally two-dimensional (2D) bluff body has been a classical problem in fluid mechanics. Commonly used bluff bodies include cylinders with circular and square cross-sectional shapes, for which the flow is governed by a single dimensionless parameter, i.e. the Reynolds number Re (= UL/ν), defined based on the incoming flow velocity (U), the length scale of the cylinder perpendicular to the incoming flow (L), and the kinematic viscosity of the fluid (ν). For a circular cylinder, the length scale is the diameter of the cylinder,

[†]Correspondence author: hongyi.jiang@uwa.edu.au

commonly denoted *D*. For a square cylinder, the length scale depends on the flow incidence angle. For a square cylinder aligned with the four sides perpendicular and parallel to the incoming flow, which is commonly referred to as a square cylinder with zero flow incidence/attack angle (e.g. Tong et al., 2008; Sheard et al., 2009; Yoon et al., 2010) or simply a square cylinder (e.g. Robichaux et al., 1999; Sohankar et al., 1999; Blackburn and Lopez, 2003), the length scale is the side length of the cylinder, commonly also denoted *D*. On the other hand, for a square cylinder aligned with all four sides 45° to the incoming flow, i.e. with an incidence angle $\alpha = 45°$ and commonly referred to as a diamond cylinder, the length scale, commonly denoted *h* (e.g. Sheard et al., 2009; Yoon et al., 2010), is $\sqrt{2}$ times the side length of the cylinder. To be consistent with previous studies, the present study uses the terms "square cylinder" and "diamond cylinder" for the cases with $\alpha = 0°$ and 45°, respectively.

Three-dimensional (3D) wake transitions for a circular and a square cylinder have been studied extensively in the literature through physical experiments, linear/nonlinear stability analyses, and direct numerical simulations (DNS). With the increase in *Re*, there appear a few wake transition regimes.

(i) At *Re* ~ 190 for a circular cylinder (Barkley and Henderson, 1996; Williamson, 1996) and *Re* ~ 165 for a square cylinder (Sheard et al., 2009; Choi et al., 2012; Park and Yang, 2016), the wake transitions from 2D to 3D through the mode A instability that originates in the primary vortex cores (Williamson, 1996; Leweke and Williamson, 1998; Thompson et al., 2001). The mode A instability is subcritical in nature and contains a small hysteresis loop (Henderson and Barkley, 1996; Henderson, 1997; Akbar et al., 2011). The mode A streamwise vortices display an out-of-phase sequence (Williamson, 1996) and a relatively large spanwise wavelength/period of ~ 4*D* for a circular cylinder (Barkley and Henderson, 1996) and ~ 5*D* for a square cylinder (Choi et al., 2012; Park and Yang, 2016). The ordered mode A structure is unstable over time and will evolve spontaneously into a more stable pattern with vortex dislocations (Williamson, 1996). For *Re* ~ 190 – 230 for a circular cylinder (Williamson, 1996) and *Re* ~ 165 – 185 for a square cylinder (Jiang et al., 2018a), the fully developed wake is represented by the pattern of mode A with vortex dislocations.

(ii) Over *Re* ~ 230 – 265 for a circular cylinder (Williamson, 1996; Barkley et al., 2000; Sheard et al., 2003) and *Re* ~ 185 – 210 for a square cylinder (Jiang et al., 2018a), the wake transitions gradually from the pattern of mode A with vortex dislocations to mode B. The mode B instability differs from the mode A instability in that it originates in the braid shear layer region (Williamson, 1996; Leweke and Williamson, 1998; Thompson et al., 2001) and is supercritical in nature (Henderson, 1997). The mode B streamwise vortices display an in-phase sequence (Williamson, 1996) and a relatively small spanwise wavelength/period of

~ 0.8D for a circular cylinder (Barkley and Henderson, 1996) and ~ 1.1D for a square cylinder (Choi et al., 2012; Park and Yang, 2016).

(iii) At Re ~ 265 for a circular cylinder (Williamson, 1996; Barkley et al., 2000; Sheard et al., 2003) and Re ~ 210 for a square cylinder (Jiang et al., 2018a), the pattern of mode A with vortex dislocations disappears, and, beyond which, the mode B structures become increasingly disordered, such that the wake becomes increasingly turbulent/chaotic. In particular, for a circular cylinder a critical condition is observed at Re ~ 265, where the mode B structures are particularly ordered, and a local peak or trough is observed for a number of flow properties, e.g. the base pressure coefficient and the Strouhal number (Williamson, 1996).

An equally important case to the square cylinder is the diamond cylinder. Among the range of flow incidence angles, the square and diamond cylinders are the two special cases where the cross-sectional shape of the cylinder is symmetric about the wake centreline. In addition, at an Re corresponding to the wake transition from 2D to 3D, the 2D wakes of both cylinders possess the Z_2 spatiotemporal symmetry, i.e. spatial reflection of the flow about the wake centreline after time evolution of every half vortex shedding period (Blackburn and Sheard, 2010; Yoon et al., 2010). Consistently, over the range of flow incidence angles, the cases of square and diamond cylinders correspond to local minima of Re for the onset of 3D (specifically mode A) wake instability (Sheard et al., 2009; Yoon et al., 2010), i.e. the square and diamond cylinders are locally most unstable to the 3D instability.

However, the 3D wake transition process of a diamond cylinder is far less studied than that of a square or circular cylinder. The most well-understood aspect for a diamond cylinder is the onset of three-dimensionality, which is identified as the mode A instability at the critical Re (Re_{cr}) with the corresponding most unstable spanwise wavelength (λ_{cr}/h) of (Re_{cr}, λ_{cr}/h) = (116, 4.0) by Sheard et al. (2009) and (120, 4.2) by Yoon et al. (2010) through Floquet stability analysis, and $Re_{cr} = 127 \pm 2$ by Tong et al. (2008) through physical experiments. Beyond Re_{cr}, Floquet analysis has been routinely adopted in the literature in identifying additional instability modes in the cylinder wake. However, for a diamond cylinder the 2D base flow becomes aperiodic at $Re \gtrsim 140$, which inhibits the application of Floquet analysis to higher Re values for the identification of additional instability modes other than mode A (Sheard et al., 2009). Alternatively, limited experimental and 3D DNS cases (Tong et al., 2008; Yoon et al., 2012; Jiang et al., 2018b) shed light on the wake structures beyond Re_{cr}. Tong et al. (2008) conducted physical experiments and identified a further wake transition from the mode A regime (with vortex dislocations) to the mode B regime at Re = 190. Yoon et al. (2012) performed 3D DNS at a few Re values and observed ordered mode A structures at Re = 150, disordered mode A structures at Re = 200, and hardly identifiable structures at Re = 250. Jiang et al. (2018b) performed 3D DNS and observed mode B structures at $Re \gtrsim 200$.

However, the wake structures reported by the above-mentioned studies do not agree well, and it is unclear whether the wake transition from mode A to mode B is a sudden or a gradual process.

In light of the earlier works, the present study aims at investigating in detail the wake transition process of a diamond cylinder based on 3D DNS with a fine increment of *Re* of 10. A particular focus will be the gradual wake transition from mode A to mode B and the corresponding variations in the hydrodynamic forces.

The present study is also motivated by the aperiodicity of the base flow for a diamond cylinder and the consequent limitation to the Floquet stability analysis (Sheard et al., 2009). As will be shown in section 3.5, the aperiodicity of the base flow arises from the transition from the primary (Kármán) vortex street to the secondary vortex street within the relatively near wake (e.g. within 15*D* downstream of the cylinder for $Re \geq 200$). Therefore, interactions between the 3D wake transition and the 2D base-flow transition may be expected for the case of a diamond cylinder. Similar cases involving the base-flow transition relatively close to the cylinder include a thin rectangular cylinder (Saha, 2007), a thin elliptical cylinder (Thompson et al., 2014), a triangular cylinder (Ng et al., 2016), etc. In contrast, for the cases of circular and square cylinders, the base flows over the 3D wake transition regimes do not transition to the secondary vortex street within at least 50*D* downstream of the cylinder (e.g. Jiang and Cheng, 2019), such that the 3D wake transition and the 2D base-flow transition are decoupled.

In the present study, the diamond cylinder serves as a representative case in investigating the interactions between the 3D wake transition and the 2D base-flow transition. In addition to the 3D DNS, Floquet analysis is employed in providing a more thorough understanding of the interactions. The Floquet analysis will be conducted with caution, where the aperiodicity of the base flow will be tackled by particular measures.

2. Numerical model

2.1. Numerical method

Direct numerical simulations were conducted in this study in solving the flow around a diamond cylinder. The governing equations are the continuity and incompressible Navier–Stokes equations:

$$\frac{\partial u_i}{\partial x_i} = 0, \tag{2.1}$$

$$\frac{\partial u_i}{\partial t} + u_j \frac{\partial u_i}{\partial x_j} = -\frac{1}{\rho}\frac{\partial p}{\partial x_i} + \nu \frac{\partial^2 u_i}{\partial x_j \partial x_j}, \tag{2.2}$$

where $(x_1, x_2, x_3) = (x, y, z)$ are the Cartesian coordinates, u_i is the velocity component in the direction x_i, t is time, p is pressure, and ν is kinematic viscosity. The numerical simulations were performed with an open-source code OpenFOAM (www.openfoam.org). The finite volume method (FVM) and the PISO (Pressure Implicit with Splitting of Operators) algorithm (Issa, 1986) were used for solving the

equations. The convection, diffusion and time derivative terms were discretized, respectively, using a fourth-order cubic scheme, a second-order linear scheme, and a blended scheme consisting of the second-order Crank-Nicolson scheme and a first-order Euler implicit scheme. The same numerical approach was used in Jiang et al. (2016, 2018a) for the simulations of wake transition of a circular and a square cylinder.

2.2. Computational domain and mesh

A hexahedral computational domain, as sketched in Fig. 1(a), was used for the present DNS. As shown in Fig. 1(a), the centre of the diamond cylinder was placed at (x, y) = (0, 0). The computational domain size was $-40 \leq x/h \leq 40$ in the streamwise direction, $-40 \leq y/h \leq 40$ in the transverse direction, and $0 \leq z/h \leq 12$ in the spanwise direction. The spanwise domain size L_z/h = 12 was chosen based on Jiang et al. (2017a), who examined the effect of L_z on the numerical modelling of flow past a circular cylinder over the 3D wake transition regimes, and demonstrated that an L_z of approximately three times the intrinsic wavelength of mode A is required to avoid inaccurate vortex patterns induced by the restriction of L_z. For the present case of a diamond cylinder, the spanwise wavelength of mode A at the onset of flow three-dimensionality is 4.00h (see section 2.4), such that L_z/h = 12 was used to accommodate three spanwise periods of mode A.

The boundary conditions for the velocity included a uniform velocity (u_x, u_y, u_z) = (U, 0, 0) at the inlet, a Neumann condition (i.e. zero normal gradient) at the outlet, and a no-slip condition on the cylinder surface. The boundary conditions for the pressure included a Neumann condition for the inlet and cylinder surface, and a reference of p = 0 at the outlet. Symmetry boundary conditions were applied at the top and bottom boundaries, while periodic boundary conditions were employed at the two lateral boundaries perpendicular to the cylinder span. The periodic boundary conditions allow for travelling waves in the spanwise direction (Jiang et al., 2017a) and follow the nature of the underlying instability modes which are spanwise-periodic (e.g. Henderson, 1997; Sheard et al., 2009). The internal flow followed an impulsive start.

(a)

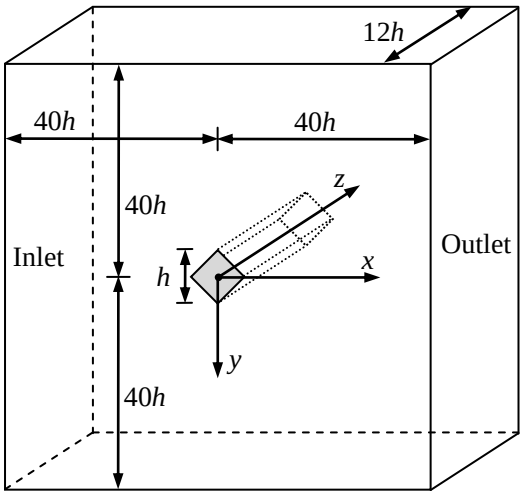

(b)

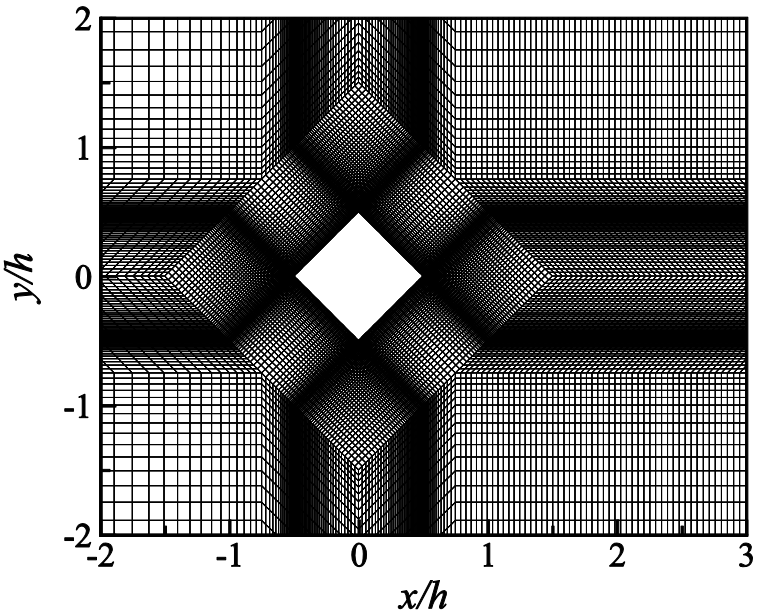

Fig. 1. (a) Schematic model of the computational domain (not to scale), and (b) Close-up view of the 2D mesh near the cylinder.

The 2D mesh in the *x*-*y* plane consisted of 92,828 cells. Fig. 1(b) shows a close-up view of the 2D mesh near the cylinder. The cylinder surface was discretised with 128 nodes. The height of the first layer of mesh next to the cylinder was 0.008*h*, which resulted in the smallest cell size at the four corners of the cylinder being 0.008*h*×0.008*h*. A relatively high resolution was used in the wake region by specifying the streamwise cell size at the wake centreline ($y = 0$) increasing linearly from 0.04*h* at $x/h = 1.5$ to 0.1*h* at $x/h = 20$. The 3D mesh was constructed by replicating the 2D mesh along the *z*-direction with a spanwise cell size $\Delta z = 0.1h$.

For each case, the time step size was fixed at $\Delta tU/h = 0.00186$, which corresponded to a Courant–Friedrichs–Lewy (CFL) limit of 0.5. The CFL number is defined as

$$\mathrm{CFL} = \frac{|u|\Delta t}{\Delta l}, \tag{2.3}$$

where $|u|$ is the magnitude of the velocity through a cell, and Δl is the cell size in the direction of the velocity.

2.3. Mesh convergence

Based on the reference mesh introduced in section 2.2, a mesh dependence study was performed at $Re = 250$ (the largest *Re* for the present DNS by OpenFOAM) with two variations.

(i) A mesh refined in the *z*-direction, where Δz was reduced from 0.1*h* to 0.05*h*.

(ii) A mesh refined in the *x*-*y* plane, where the numbers of cells in both the *x*- and *y*-directions were 1.5 times those of the reference mesh, while the

general topology of the mesh remained unchanged. In particular, the number of cells around the cylinder surface was increased by 1.5 times, while the height of the first layer of mesh next to the cylinder was reduced by 1.5 times. For this case, the time step size was also reduced by 1.5 times so as to satisfy the CFL limit of 0.5.

Table 1 lists some major flow properties calculated with the three meshes. The drag and lift coefficients (C_D and C_L) and the Strouhal number (St) are defined as:

$$C_D = \frac{F_D}{\frac{1}{2}\rho U^2 h L_z}, \tag{2.4}$$

$$C_L = \frac{F_L}{\frac{1}{2}\rho U^2 h L_z}, \tag{2.5}$$

$$St = \frac{f_L h}{U}, \tag{2.6}$$

where F_D and F_L are the drag and lift forces on the cylinder, respectively, and f_L is the frequency of the fluctuating lift force, which is determined as the peak frequency derived from the fast Fourier transform (FFT) of the time history of C_L. The time-averaged drag and lift coefficients are denoted $\overline{C_D}$ and $\overline{C_L}$, respectively. The root-mean-square lift coefficient is calculated as:

$$C_L' = \sqrt{\frac{1}{N}\sum_{i=1}^{N}\left(C_{L,i} - \overline{C_L}\right)^2}, \tag{2.7}$$

where N is the number of values in the time history. The wake recirculation length (L_r) is defined as the horizontal distance between the centre of the cylinder ($x/h = 0$) and the wake stagnation point, which is averaged over both time and the cylinder span. For each case listed in Table 1, the time average was performed for at least 650 non-dimensional time units (defined as $t^* = tU/h$), after discarding an initial period of at least 350 non-dimensional time units.

As shown in Table 1, the flow properties calculated with the two refined meshes are very close to those calculated with the reference mesh.

Table 1. Mesh dependence check of some major flow properties for Re = 250. The results other than the reference case are shown by the relative differences with respect to those of the reference case.

Case	$\overline{C_D}$	C_L'	St	L_r/h
Reference	1.7213	0.4691	0.1800	1.3487
Refined in the z-direction	+ 0.34%	– 0.11%	+ 0.46%	– 0.76%
Refined in the x-y plane	+ 0.98%	+ 3.71%	+ 0.87%	– 1.59%

In addition, for the three cases listed in Table 1, Fig. 2 shows the time-averaged and root-mean-square velocity profiles sampled at a few streamwise locations in the

wake. The velocity profiles were also averaged over the cylinder span. The time-averaged streamwise and transverse velocities are denoted as $\overline{u_x}$ and $\overline{u_y}$, respectively, while the root-mean-square streamwise and transverse velocities are calculated as:

$$u_x' = \sqrt{\frac{1}{N}\sum_{i=1}^{N}\left(u_{x,i} - \overline{u_x}\right)^2}\,, \tag{2.8}$$

$$u_y' = \sqrt{\frac{1}{N}\sum_{i=1}^{N}\left(u_{y,i} - \overline{u_y}\right)^2}\,. \tag{2.9}$$

As shown in Fig. 2, the velocity profiles calculated with the two variation cases agreed well with those calculated with the reference case, with the largest difference at any (x, y) location being smaller than 0.02U. Based on the results shown in Table 1 and Fig. 2, the reference mesh was considered adequate and was adopted for the present study.

(a)

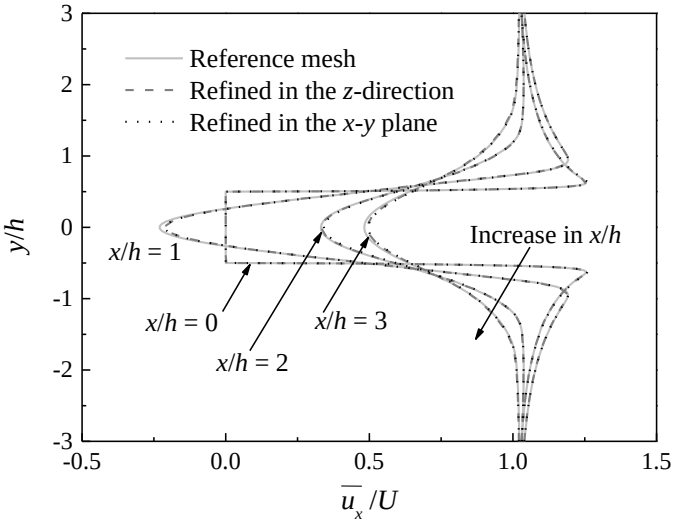

(b)

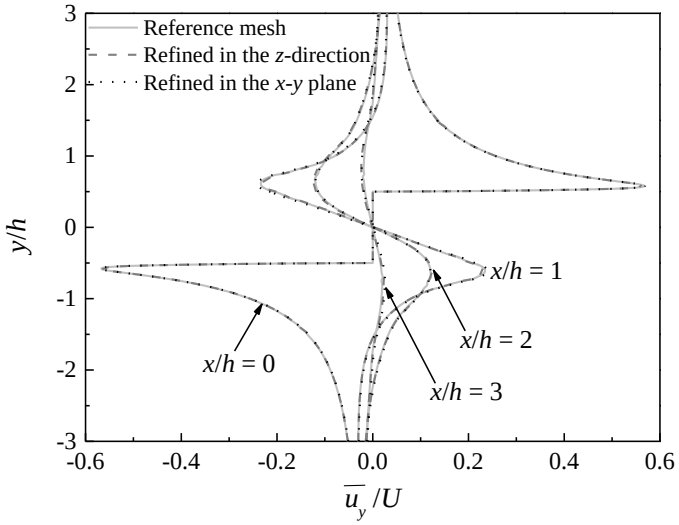

(c)

(d)

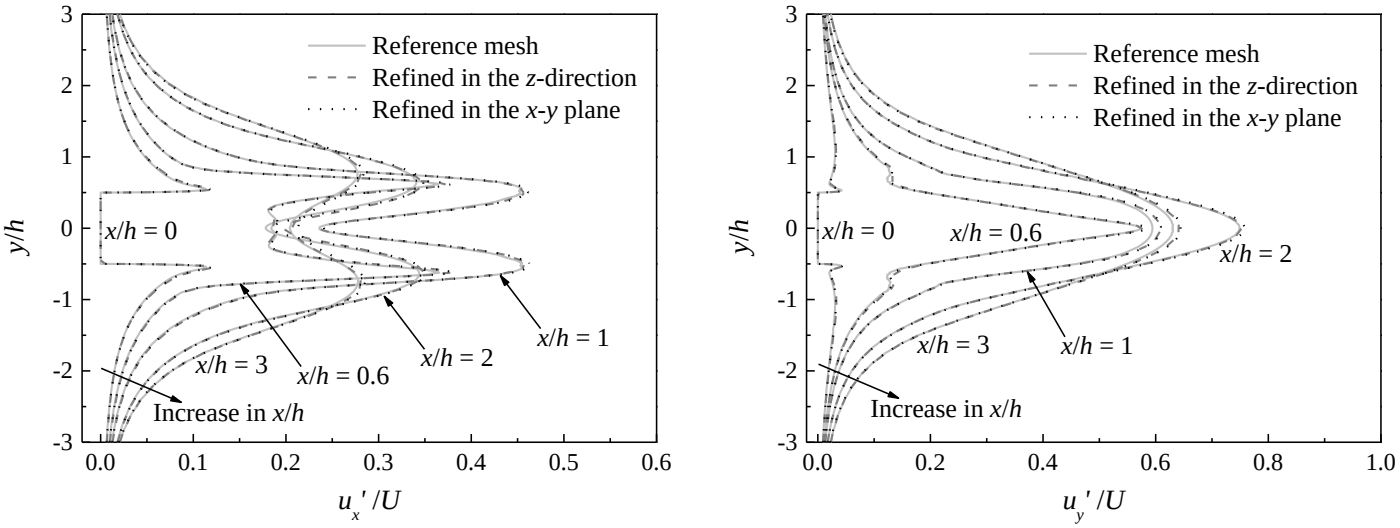

Fig. 2. Mesh dependence check of the velocity profiles sampled at a few streamwise locations for Re = 250: (a) time-averaged streamwise velocity profiles, (b) time-averaged transverse velocity profiles, (c) root-mean-square streamwise velocity profiles, and (d) root-mean-square transverse velocity profiles. The velocity profiles were also averaged over the cylinder span.

2.4. Onset of three-dimensionality

For flow past a diamond cylinder, the flow transitions from 2D to 3D through the mode A wake instability (Tong et al., 2008; Sheard et al., 2009; Yoon et al., 2010). Floquet stability analysis has been a preferred method in determining the Re_{cr} and λ_{cr} values for this instability, e.g. (Re_{cr}, λ_{cr}/h) = (116, 4.0) by Sheard et al. (2009) and (120, 4.2) by Yoon et al. (2010). In this section, Floquet analysis was used to confirm the (Re_{cr}, λ_{cr}/h) values and to map out the neutral instability curve for mode A. The present Floquet analysis followed the methodology presented in Barkley and Henderson (1996) and the numerical framework embedded in the open-source code Nektar++ (Cantwell et al., 2015) (since Floquet analysis is not readily available in the standard framework of OpenFOAM but has been well tested in Nektar++). The computational domain size used in Nektar++ for the Floquet analysis was the same as that introduced in section 2.2 for OpenFOAM. The macro-element mesh for Nektar++ used 32 macro-elements around the cylinder perimeter, $0.0388h \times 0.0388h$ for the smallest cell size at the four corners of the cylinder, and a relatively high wake resolution such that the streamwise cell size at the wake centreline increased linearly from $0.196h$ at x/h = 1.5 to $0.810h$ at x/h = 40. Overall, the macro-element mesh was approximately 4 to 5 times coarser in both the x- and y-directions than the mesh used in OpenFOAM. The macro-elements were then subdivided using fifth-order Lagrange polynomials (N_p = 5) on the Gauss–Lobatto–Legendre points for the quadrilateral expansions. Owing to the use of the high-order spectral/hp element method for Nektar++ (Karniadakis and Sherwin, 2005), the overall mesh resolution for Nektar++ was finer than that for the FVM-based OpenFOAM.

Fig. 3(a) shows the dependence of the dominant Floquet multiplier μ on the

spanwise wavenumber β (= $2\pi/\lambda$) for Re = 120 and 140, together with similar results predicted by Sheard et al. (2009) and Yoon et al. (2010). In Fig. 3(a), a single peak region of $|\mu| > 1.0$ is observed, where the μ values are real and positive, which suggests that this peak region corresponds to the mode A instability. Fig. 3(b) shows the neutral instability curve of mode A. The (Re_{cr}, λ_{cr}/h) values for the present Floquet analysis are determined based on a linear interpolation of the peak $|\mu|$ values at Re = 121 and 122 to the neutral instability of $|\mu| = 1.0$. The results (Re_{cr}, λ_{cr}/h) = (121.3, 4.09) agree well with those reported by Sheard et al. (2009) and Yoon et al. (2010). In addition, a mesh convergence check was performed at (Re, λ/h) = (120, 4.107), where an increase in N_p from 5 to 7 resulted in a decrease in $|\mu|$ of 0.01%, suggesting the use of N_p = 5 was adequate.

(a)

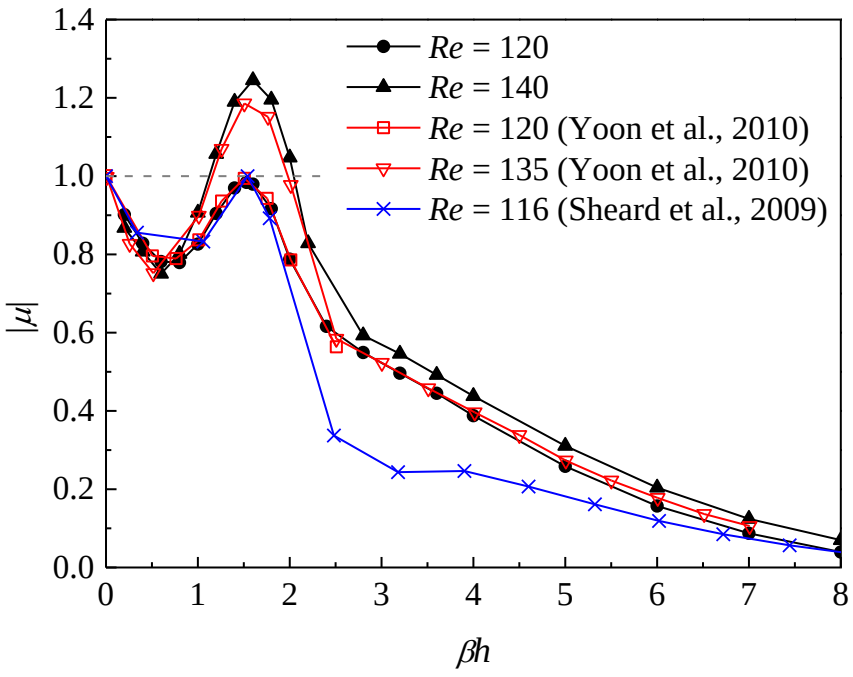

(b)

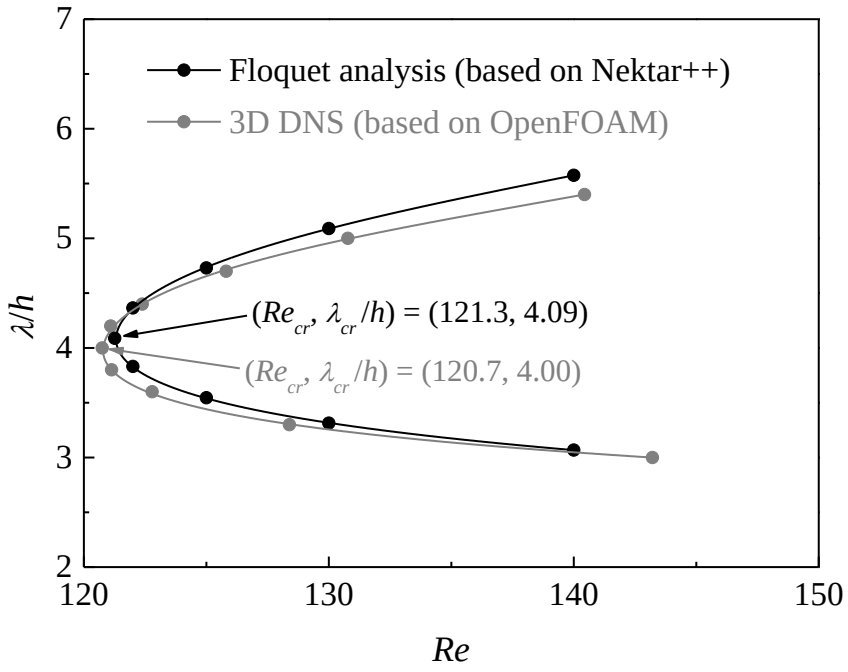

Fig. 3. Floquet stability analysis results: (a) Dependence of the dominant Floquet multiplier μ on the spanwise wavenumber β, and (b) The neutral instability curve of mode A.

As shown in Fig. 3(b), the neutral instability curve for mode A was also calculated through 3D DNS (based on OpenFOAM). For the DNS method, only a half of a spanwise period of the mode A structure was simulated (by using $L_z = \lambda/2$, $L_z/\Delta z = 10$ and symmetry boundary conditions at the two lateral boundaries to isolate a half of a spanwise period of mode A), such that the computational cost of this method was comparable to that of the Floquet analysis. More details on this method can be found in Jiang et al. (2017b). The present DNS method predicted $(Re_{cr}, \lambda_{cr}/h) = (120.7, 4.00)$, which agreed well with the results predicted by the Floquet analysis. In addition, a mesh convergence check at $L_z = \lambda/2 = 2h$ showed that by (i) doubling the mesh layers in the spanwise direction (to $L_z/\Delta z = 20$), (ii) doubling the cell numbers in both the x- and y-directions, or (iii) doubling the domain size in the x-y plane (to $-80 \le x/h \le 80$ and $-80 \le y/h \le 80$), the variations in Re_{cr} were all within 1%. In particular, variation case (i) predicted also $Re_{cr} = 120.7$. For the 3D wake transition process investigated in section 3, the mesh resolution used in OpenFOAM was identical to that used in the variation case (i), such that $(Re_{cr}, \lambda_{cr}/h) = (120.7, 4.00)$ was directly applicable to the OpenFOAM cases examined in section 3.

3. Numerical results

3.1. Three-dimensional wake transition

In the present study, the 3D wake transition beyond $Re_{cr} = 120.7$ was examined up to $Re = 250$. For each Re, the flow was deemed fully developed after a time

integration of 1000 non-dimensional time units, which corresponded to ~ 180 vortex shedding cycles. After that, at least another 1000 non-dimensional time units were used for the statistics and analysis of the fully developed flow. The wake transition process was identified through visualising the streamwise and spanwise vorticity (ω_x and ω_z) fields, where ω_x and ω_z are defined in a non-dimensional form as

$$\omega_x = \left(\frac{\partial u_z}{\partial y} - \frac{\partial u_y}{\partial z} \right) \frac{h}{U}, \tag{3.1}$$

$$\omega_z = \left(\frac{\partial u_y}{\partial x} - \frac{\partial u_x}{\partial y} \right) \frac{h}{U}. \tag{3.2}$$

Fig. 4 illustrates the streamwise and spanwise vortex structures for *Re* in different wake transition regimes. In summary, with the increase in *Re*, the wake undergoes a transition sequence of "mode A with global vortex dislocations ($Re = Re_{cr} - 150$) → mode swapping between modes A and B ($Re = 160 - 210$) → mode B ($Re \geq 220$)".

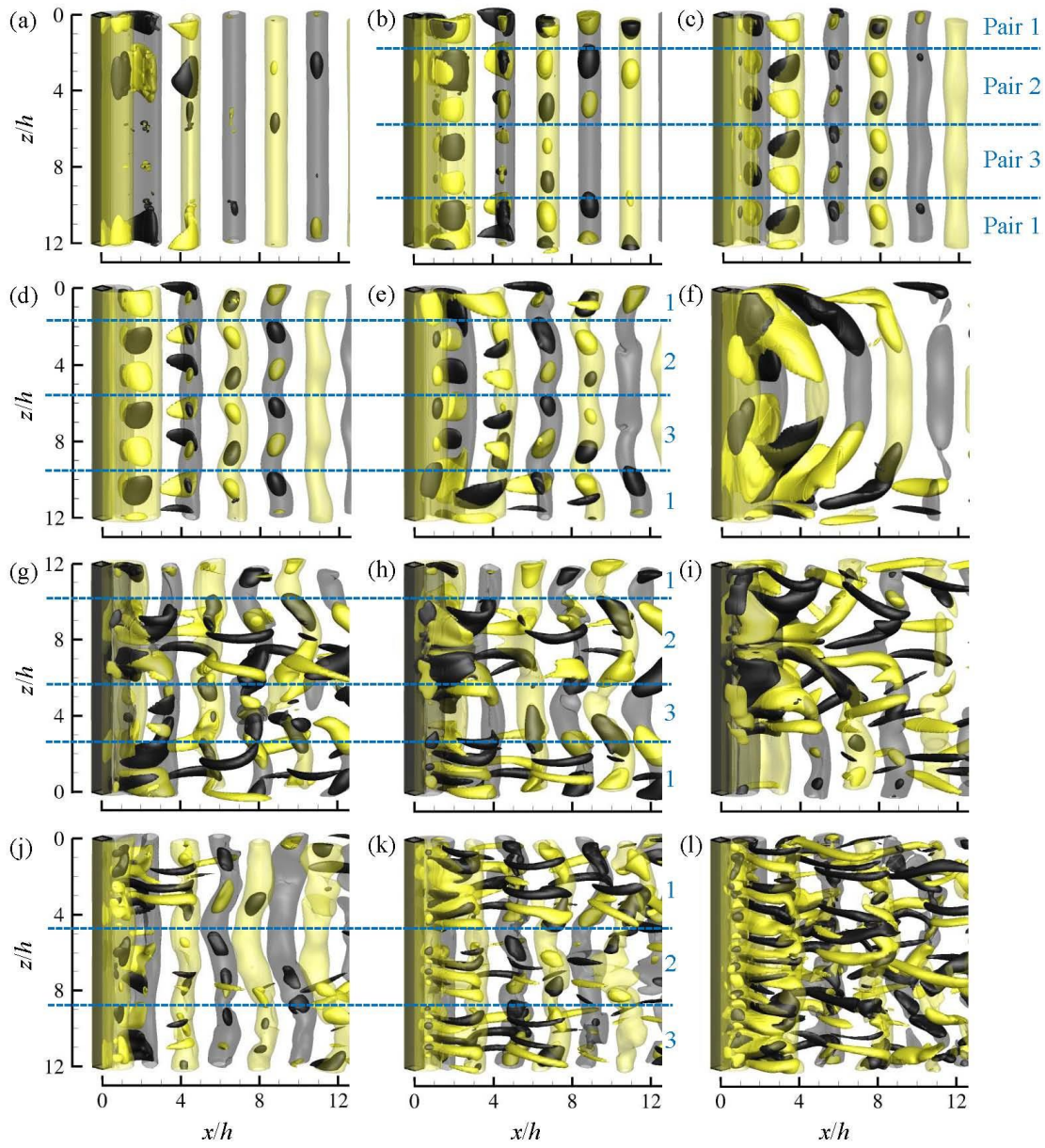

Fig. 4. Instantaneous vorticity fields in the near wake of a diamond cylinder for (a) – (f) Re = 125 with t^* = 80, 120, 320, 400, 480 and 520, (g) – (i) Re = 150 with t^* = 1605, 1645 and 1675, (j) – (k) Re = 190 with t^* = 1360 and 1380, and (l) Re = 240 with t^* = 2125. The translucent iso-surfaces represent spanwise vortices with $\omega_z = \pm 1.0$, while the opaque iso-surfaces represent streamwise vortices with $\omega_x = \pm 0.02$ for panels (a) and (b), $\omega_x = \pm 0.3$ for panel (c), $\omega_x = \pm 0.5$ for panels (d) – (f), $\omega_x = \pm 0.8$ for panels (g) – (i), and $\omega_x = \pm 1.0$ for panels (j) – (l). Dark grey and light yellow denote positive and negative vorticity values, respectively. The flow is from left to right past the cylinder on the left.

Specifically, for $Re = Re_{cr} - 150$, the initial 3D structure developed in the wake is a relatively ordered mode A structure (Fig. 4b–d). As shown in Fig. 4(b–d), the mode A structure originates and grows from the primary vortex cores, which is consistent with the origin of the mode A instability identified based on a circular cylinder

(Williamson, 1996; Leweke and Williamson, 1998; Thompson et al., 2001). With the evolution over time, the relatively ordered mode A structure evolves into a pattern with vortex dislocations (Fig. 4d–f). The origin of the vortex dislocations shown in Fig. 4(f) can be traced back to a slight difference in strength in the three pairs of the mode A streamwise vortices shown in Fig. 4(b–e). Ever since the emergence of the three mode A streamwise vortex pairs at $t^* \sim 100$ (from Fig. 4(a) to Fig. 4(b)), pair 1 is always slightly stronger than the other two pairs (Fig. 4b–e). With the evolution in time, this stronger pair of mode A structure grows into a local vortex dislocation in Fig. 4(e). After that, the local vortex dislocation develops along the spanwise direction and engulfs the other two pairs of mode A structure, resulting in a pattern of global vortex dislocation for the saturated flow (Fig. 4f).

For the saturated flow, scattered mode A streamwise vortex pairs emerge intermittently. Depending on the *Re* value, the mode A streamwise vortex pairs developed in the wake (e.g. Fig. 4d,g,j) may evolve into one of the following two patterns.

(i) The mode A streamwise vortex pair evolves into a local vortex dislocation, e.g. pair 1 in Fig. 4(d,e) and pair 2 in Fig. 4(g,h).

(ii) The mode A streamwise vortex pair evolves into the mode B structure, e.g. pair 1 in Fig. 4(g) and pairs 2 and 3 in Fig. 4(j).

For $Re = Re_{cr} - 140$, only pattern (i) exists. Any particular mode A streamwise vortex pair that evolves through pattern (i) would engulf the unevolved mode A streamwise vortex pairs and lead to a pattern of global vortex dislocations (e.g. Fig. 4d–f). For $Re = 150 - 210$, both patterns exist. A special condition occurs at $Re = 150$, where although pattern (ii) exists occasionally, it is always accompanied by the co-existence of pattern (i) and would thus still evolve into global vortex dislocations (e.g. Fig. 4g–i). In summary, for $Re = Re_{cr} - 150$ the saturated flow is always represented by global vortex dislocations.

For $Re = 160 - 210$, global vortex dislocations appear intermittently in the saturated flow. Similar to $Re = 150$, any mode A streamwise vortex pair that evolves through pattern (i) would lead to global vortex dislocations, even when other mode A streamwise vortex pair(s) evolve through pattern (ii) at the same time (e.g. Fig. 4g–i). In contrast, global vortex dislocation is suppressed when all of the mode A streamwise vortex pairs evolve through pattern (ii) (e.g. Fig. 4j,k). This pattern (i)/(ii) of evolution results in an intermittent appearance of global vortex dislocations (i.e. mode swapping) for $Re = 160 - 210$.

The mode swapping over $Re = 160 - 210$ is quantified in Fig. 5. The shaded and clear blocks indicate dislocation and non-dislocation time periods, respectively, which are determined by visually examining the time evolution of the streamwise vorticity field (e.g. those shown in Fig. 4) with an interval of 10 non-dimensional time units. The global vortex dislocations are spotted easily as they appear over continuous time periods and normally occupy the entire domain (Jiang et al., 2016). Based on the time histories shown in Fig. 5, the probability of occurrence of dislocation is further quantified in Fig. 6. As shown in Fig. 6, the probability of occurrence of dislocation decreases monotonically with increasing *Re*. With the increase in *Re*, the mode B

structures are more likely to be destabilised and in turn replace/stabilise the mode A streamwise vortex pairs through the pattern (ii) evolution, which results in a reducing likelihood of pattern (i), i.e. a reducing likelihood of dislocation. It is also noticed that the mode swapping shown in Fig. 5 is most frequent when the probability of occurrence of dislocation is close to 50%.

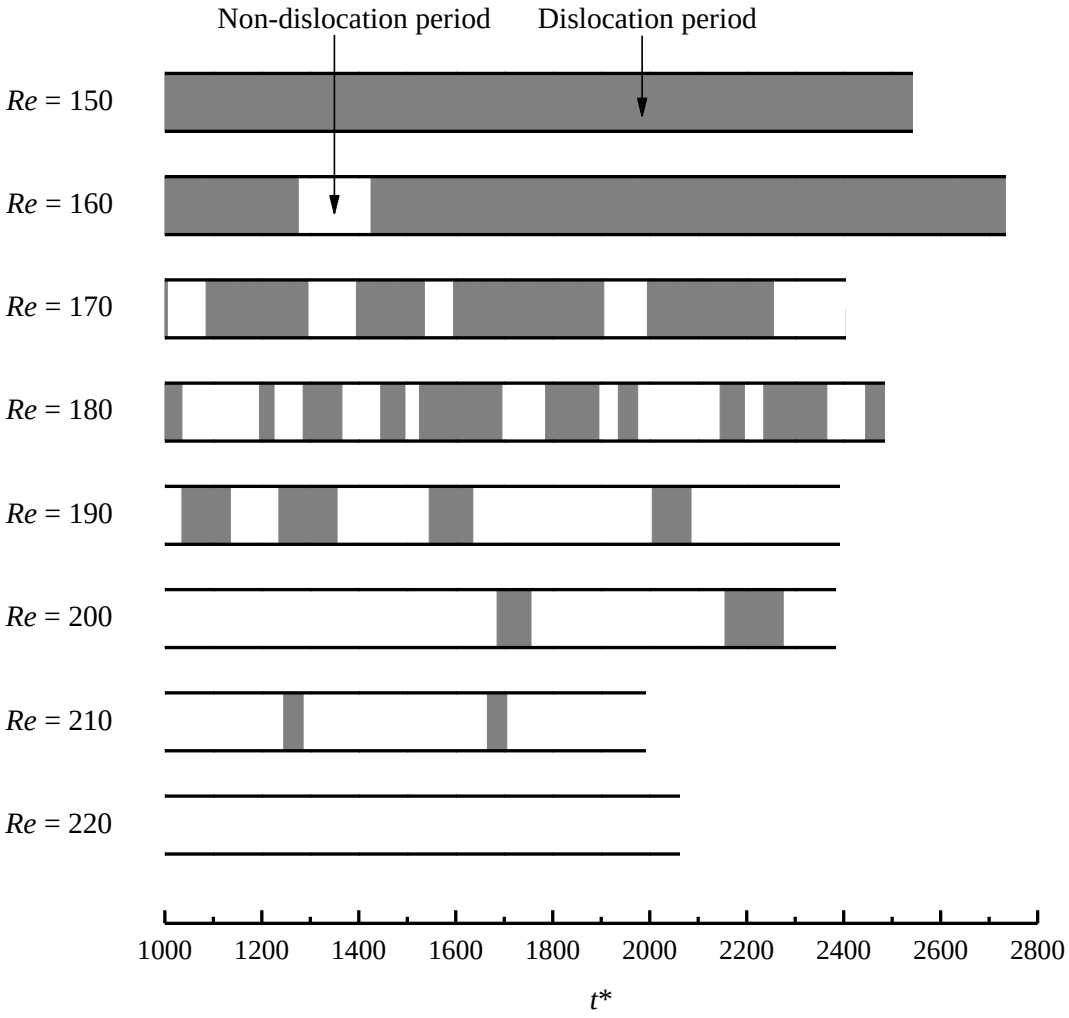

Fig. 5. Quantification of the intermittent appearance of global vortex dislocations in the range of *Re* = 150 – 220. The shaded and clear blocks indicate dislocation and non-dislocation time periods, respectively.

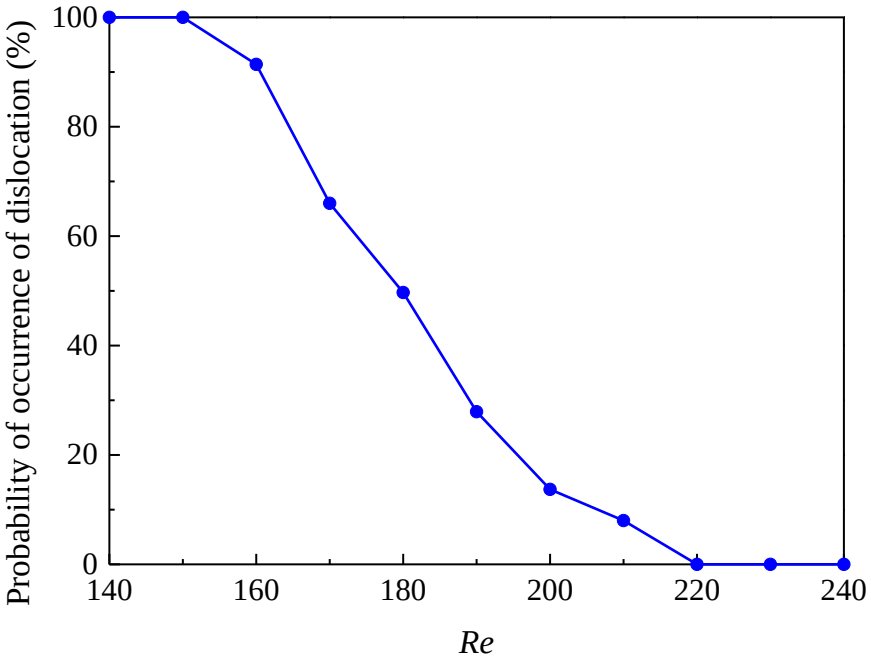

Fig. 6. Probability of occurrence of vortex dislocation for *Re* over the mode swapping regime.

For $Re \geq 220$, pattern (i) no longer exists. Scattered mode A streamwise vortex pairs, which evolve through pattern (ii) only, are observed for < 8% and < 2% of the statistical time periods for $Re = 220$ and 250, respectively, which suggests that for $Re \geq 220$ the influence of mode A is minimal. The wake is dominated by disordered mode B structures, as illustrated in Fig. 4(l).

3.2. Characteristics of the dislocation and non-dislocation periods

Based on the separation of the dislocation and non-dislocation time periods in Fig. 5, the flow properties, such as the hydrodynamic forces on the cylinder, can also be decomposed into the values corresponding to the dislocation and non-dislocation time periods. Such an analysis has not been performed before in the literature, and is expected to shed new light on the different characteristics of the dislocation and non-dislocation periods.

Fig. 7 shows the time histories of C_L for *Re* over the mode swapping regime, overlaid with shaded and clear regions representing dislocation and non-dislocation time periods, respectively. As shown in Fig. 7, the dislocation periods correspond to local reductions in the fluctuation amplitude of C_L, which include some extremely small fluctuation amplitudes over the time history. In particular, the long dislocation periods observed for $Re = 160$ consist of frequent local reductions in the fluctuation amplitude of C_L, except for the non-dislocation period at $t^* = 1280 – 1420$, where the fluctuation amplitude is sustained at a relatively large level.

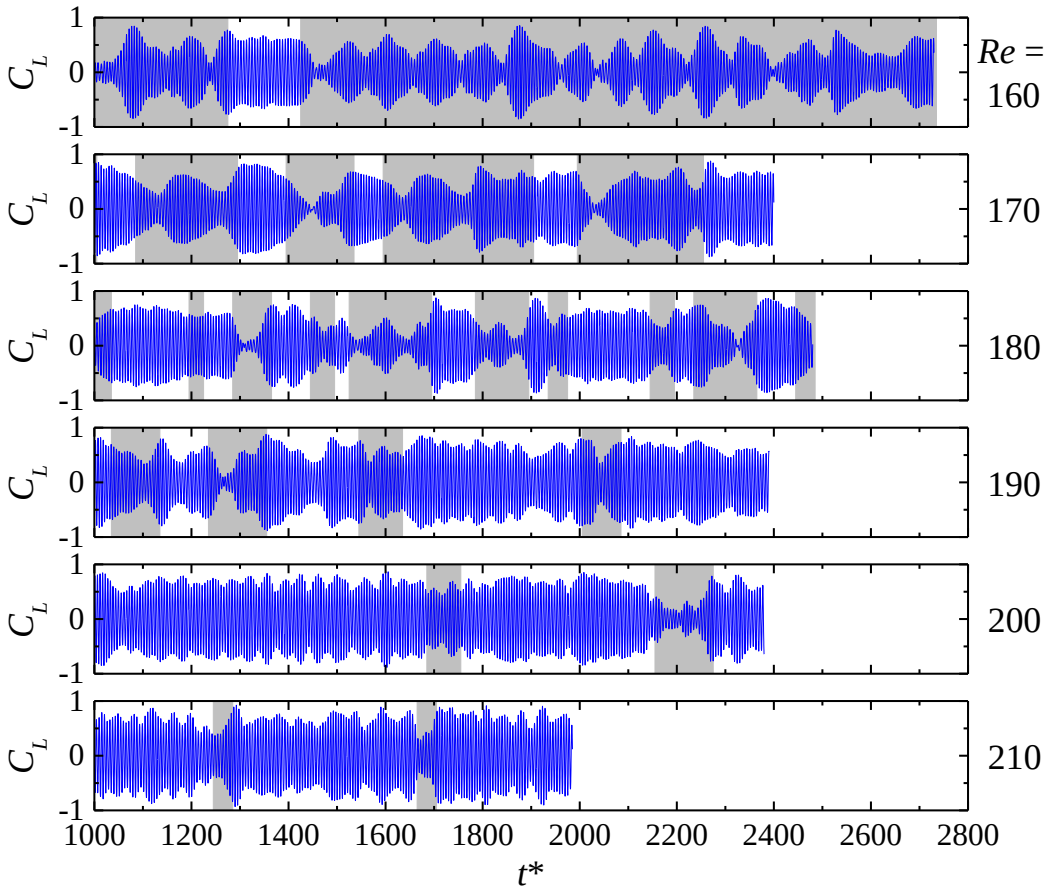

Fig. 7. Time histories of the lift coefficient for Re = 160 – 210, overlaid with shaded and clear regions representing dislocation and non-dislocation time periods, respectively.

The local reductions in the fluctuation amplitude of C_L for the dislocation periods originate from the local dislocations in the mode A streamwise vortices. As shown in Fig. 4(e,f,h,i), the local dislocations in the mode A streamwise vortices towards the upstream direction would induce an upstream movement of the corresponding fractions of the spanwise vortex rollers and eventually lead to inclined spanwise vortex rollers at the two sides of the local dislocation. The inclined spanwise vortex rollers shown in Fig. 4(f,i) indicate phase differences in the primary vortex shedding at different spanwise locations up to at least 180 °(the inclined spanwise vortex rollers may reach the streamwise location for the subsequent spanwise vortex roller), which partially cancels out the integrated lift coefficient. In contrast, the mixed modes A and B structures in the non-dislocation periods do not induce significant inclinations in the spanwise vortex rollers (e.g. Fig. 4j,k), such that the fluctuation amplitudes of C_L are relatively large.

Fig. 8(a) shows the C_L'–Re relationship over the wake transition regimes. The C_L' values over the mode swapping regime are further decomposed into the ones corresponding to the dislocation and non-dislocation time periods. As expected, the C_L' values for the dislocation periods are consistently smaller than those for the non-dislocation periods. With the gradual decrease in the probability of occurrence of

dislocation over Re = 160 – 210 (Fig. 6), the overall C_L' value moves gradually from the dislocation branch to the non-dislocation branch (Fig. 8a).

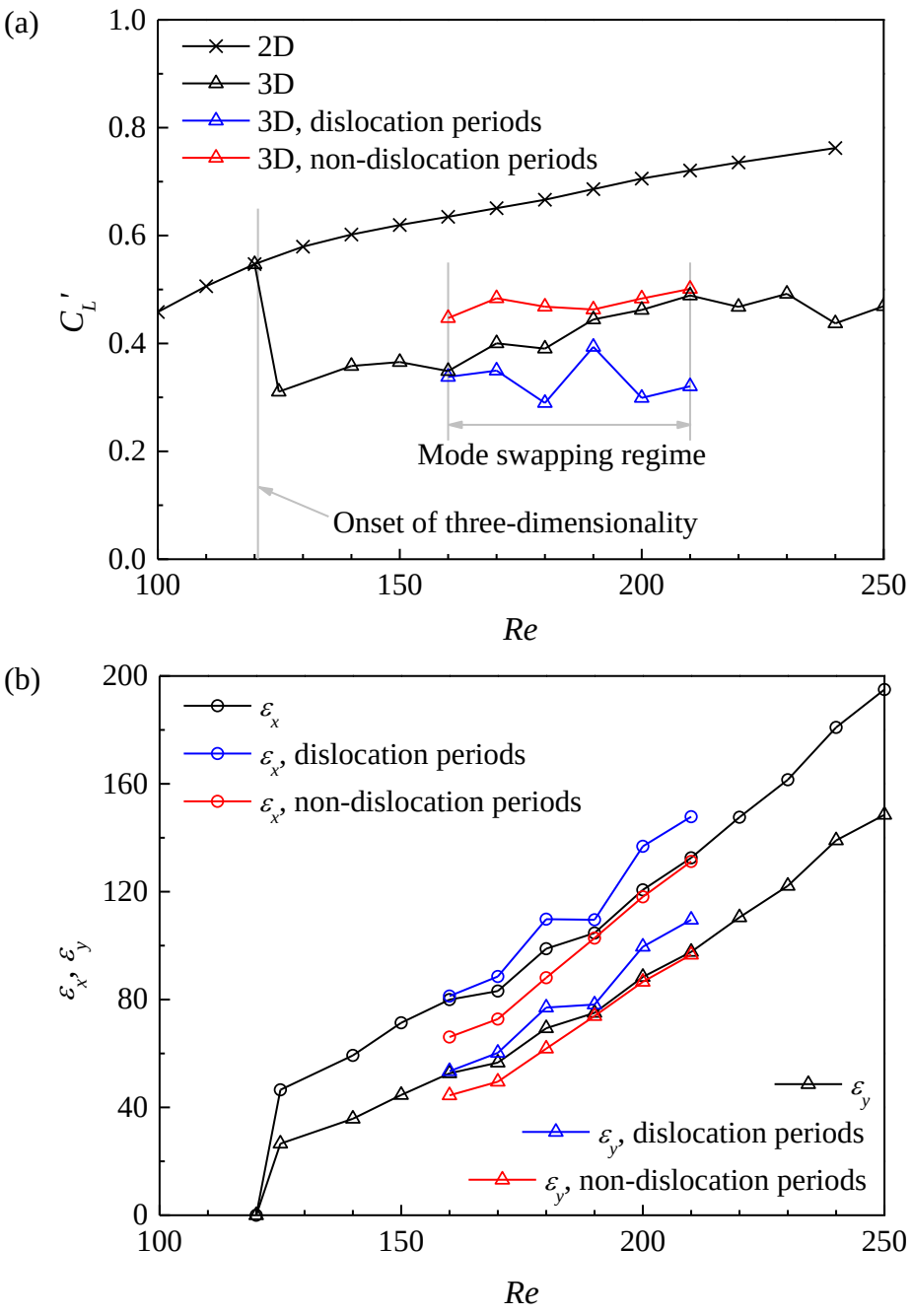

Fig. 8. (a) The C_L'–Re relationship, and (b) the ε_x–Re and ε_y–Re relationships (integrated over x/h = 0 – 20) over the wake transition regimes.

Fig. 8(b) examines the degree of flow three-dimensionality in the wake, quantified by the time-averaged streamwise and transverse enstrophies (ε_x and ε_y) defined as

$$\varepsilon_x = \frac{1}{2}\int_V \omega_x^2 \mathrm{d}V\,, \tag{3.3}$$

$$\varepsilon_y = \frac{1}{2}\int_V \omega_y^2 \mathrm{d}V\,, \qquad \text{where} \quad \omega_y = \left(\frac{\partial u_x}{\partial z} - \frac{\partial u_z}{\partial x}\right)\frac{h}{U}\,, \tag{3.4}$$

where V is the volume of the flow field of interest. The enstrophies shown in Fig. 8(b) are integrated over the wake region of x/h = 0 – 20. In general, the degree of three-dimensionality increases gradually with increasing Re. In addition, the ε_x and ε_y values over the mode swapping regime are decomposed into the ones corresponding to the dislocation and non-dislocation periods. The enstrophies for the dislocation periods are slightly larger than those for the non-dislocation periods, which suggests that the dislocation periods have larger degrees of flow three-dimensionality than the non-dislocation periods. The larger degrees of flow three-dimensionality for the dislocation periods are consistent with the larger reductions in the C_L' values from their 2D counterparts shown in Fig. 8(a).

In comparison, Fig. 9 shows the C_L'–Re and ε_x–Re relationships for flow past a circular cylinder. In the mode swapping regime of Re ~ 230 – 265 (Williamson, 1996; Barkley et al., 2000; Sheard et al., 2003; Jiang et al., 2016), the C_L' and ε_x values corresponding to the dislocation and non-dislocation periods are calculated in the present study by further analysing the numerical cases reported by Jiang et al. (2016), where the dislocation and non-dislocation time periods are identified in a similar manner to Fig. 5. Similar to the diamond cylinder, for a circular cylinder the dislocation periods also display larger degrees of flow three-dimensionality and larger reductions in C_L' (from their 2D counterparts) than the non-dislocation periods (Fig. 9).

However, a major difference between a circular and a diamond cylinder is that for a circular cylinder there is a critical condition at the upper end of the mode swapping regime (Williamson, 1996), where a local peak or trough is observed for various flow properties (see e.g. Fig. 9). In contrast, such a critical condition does not appear for a diamond cylinder (Fig. 8). Such a difference between a circular and a diamond cylinder originates from the development of particularly ordered and parallel mode B structures for the non-dislocation periods of a circular cylinder (see e.g. figure 14(c) of Jiang et al. (2016)) whereas more disordered mode B structures for the non-dislocation periods of a diamond cylinder (see e.g. Fig. 4k). For a circular cylinder, the particularly ordered mode B structures for the non-dislocation periods induce ε_x values less than half of those for the dislocation periods (Fig. 9b) and C_L' values very close to the largest possible level, i.e. their 2D counterparts (Fig. 9a). In contrast, the disordered mode B structures observed for the non-dislocation periods of a diamond cylinder induce relatively large degrees of flow three-dimensionality comparable to those of the dislocation periods (Fig. 8b) and C_L' values much smaller than their 2D counterparts (Fig. 8a). Since the non-dislocation branches shown in Fig. 8 are now closer to the dislocation branches than the 2D curves (for Fig. 8(b) the 2D results are $\varepsilon_x = \varepsilon_y = 0$), the overall C_L'–Re, ε_x–Re and ε_y–Re curves, which are bounded by the dislocation and non-dislocation branches, do not show obvious peak/trough towards their 2D counterparts at the upper end of the mode swapping regime. Instead, only slight changes in the variation trends may be observed when the overall curve

detaches the dislocation branch at *Re* ~ 160 and attaches the non-dislocation branch at *Re* ~ 210. These slight changes may easily be overlooked when the dislocation and non-dislocation branches are switched off.

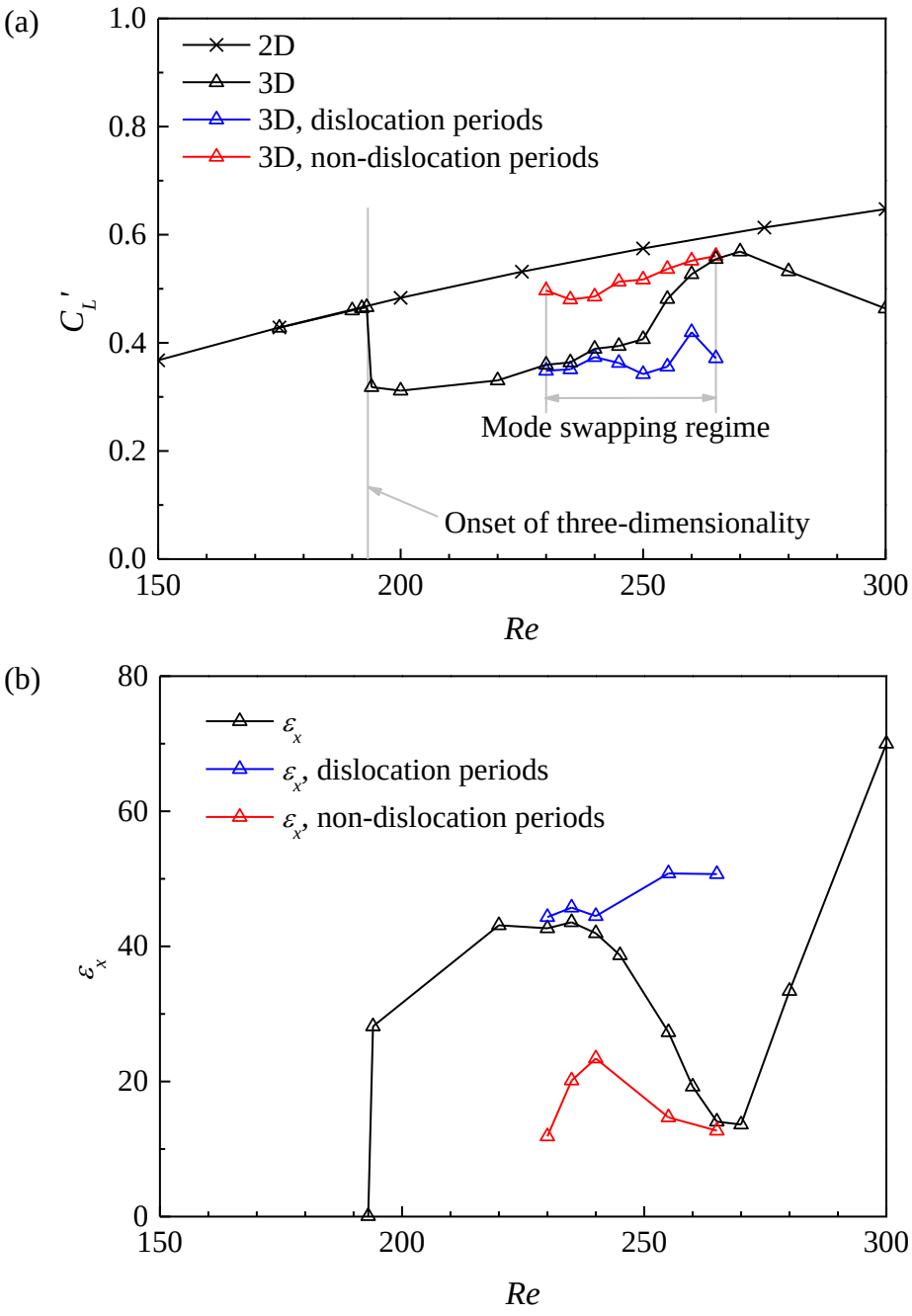

Fig. 9. (a) The C_L'–*Re* relationship, and (b) the ε_x–*Re* relationship (integrated over x/D = 0 – 10) over the wake transition regimes for flow past a circular cylinder.

3.3. Vortex shedding frequency

Fig. 10 shows the frequency spectra of C_L for the determination of the vortex shedding frequency. The frequency spectra are obtained from the FFT of the time histories of C_L. Each frequency spectrum shown in Fig. 10 contains a main peak,

accompanied by broadband frequencies at the two sides of the peak, owing to the irregularity of the 3D flows.

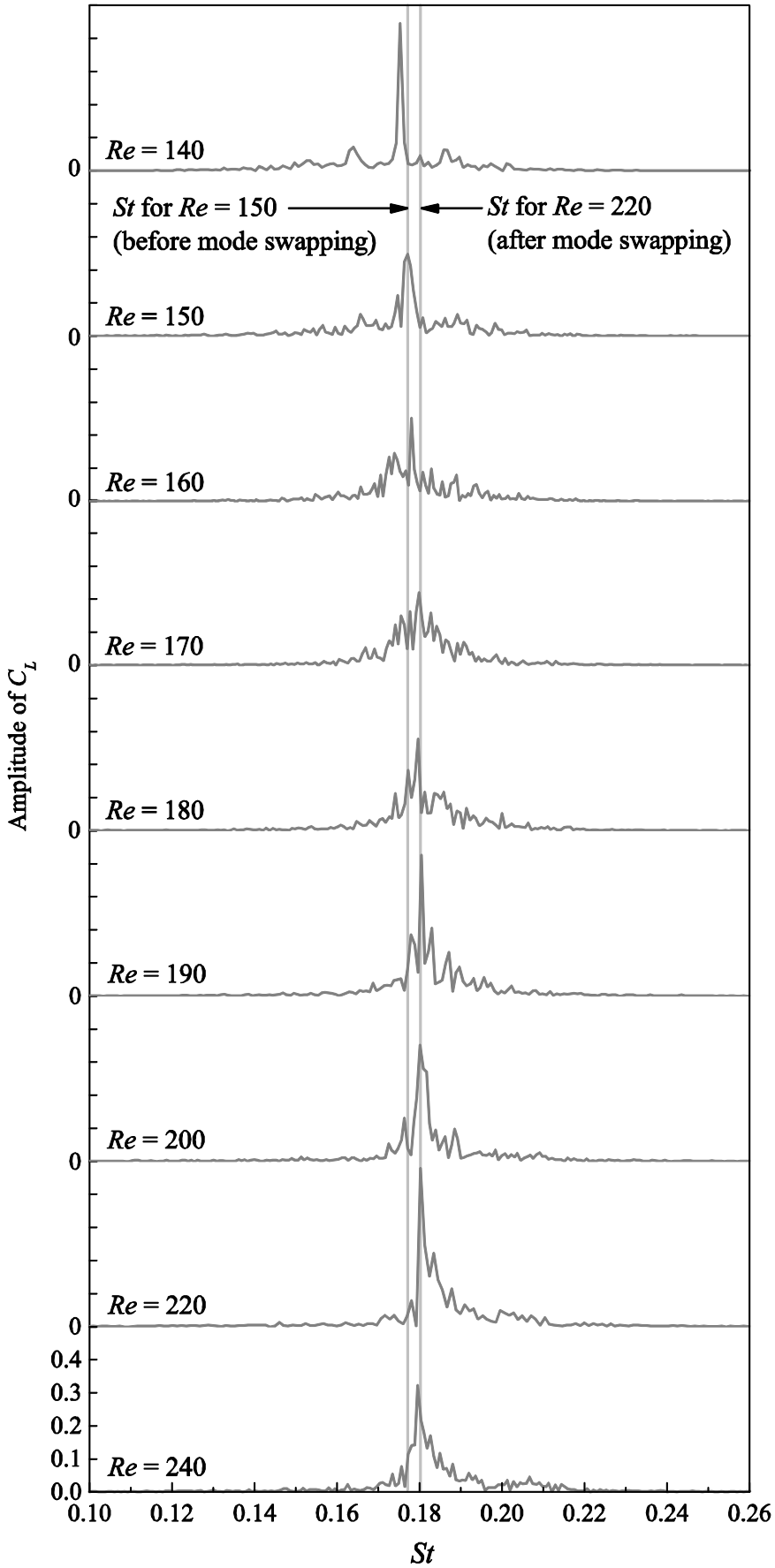

Fig. 10. Frequency spectra of C_L for Re = 140 – 240.

Based on the separation of the time history of C_L into the dislocation and non-dislocation periods in Fig. 7, the frequency spectrum of C_L can also be decomposed by performing FFT separately on the dislocation and non-dislocation ranges of the time history. Fig. 11(a) shows an example of the decomposition of the frequency spectrum of C_L for Re = 180. It is seen that the peak frequency corresponding to the non-dislocation periods is much closer to that of the dislocation periods than that calculated through 2D DNS, which is similar to the variation trends of ε_x and ε_y shown in Fig. 8(b). Jiang and Cheng (2017) also showed based on a circular cylinder that in the mode swapping regime the degree of reduction in the 3D St value from its 2D counterpart correlates well with the degree of flow three-dimensionality. In comparison, Fig. 11(b) shows a circular cylinder example at Re = 250, where the peak frequency corresponding to the non-dislocation periods is much closer to its 2D counterpart than that of the dislocation periods. For the circular cylinder, the difference between the peak frequencies corresponding to the dislocation and non-dislocation periods (of ΔSt = 0.0104) can be revealed by the frequency spectrum corresponding to the entire time history of C_L, where two peaks of ΔSt = 0.00997 apart are observed (Fig. 11b). For the diamond cylinder, however, because the difference between the peak frequencies corresponding to the dislocation and non-dislocation periods (of ΔSt = 0.00195) is even smaller than the range of St under the main frequency peak (of $\Delta St \gtrsim 0.005$), the frequency spectrum corresponding to the entire time history of C_L cannot display the twin-peaked pattern. The relatively small ΔSt between the dislocation and non-dislocation branches over the mode swapping regime can also be viewed in Fig. 10 by highlighting the peak frequencies of Re = 150 (just before mode swapping) and Re = 220 (just after mode swapping) using two vertical lines, where a similar minor difference of ΔSt = 0.00318 is observed.

(a)

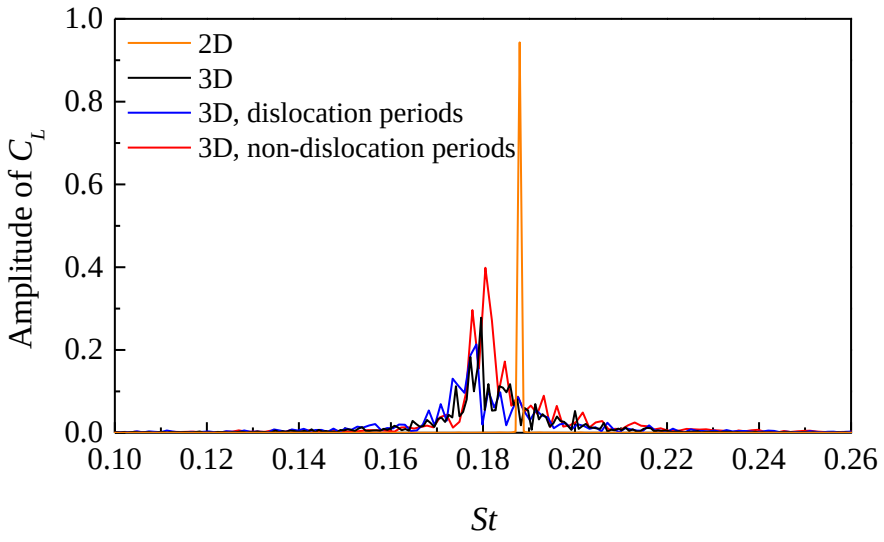

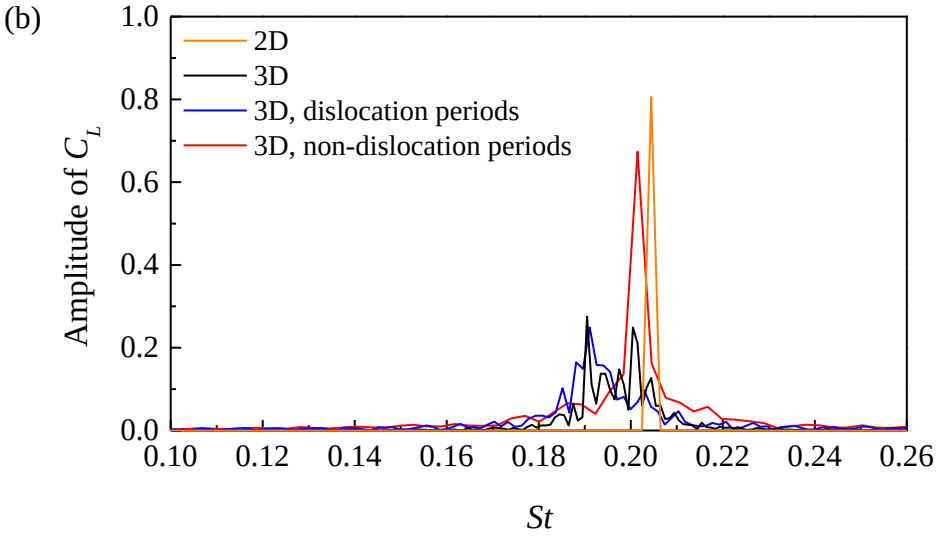

Fig. 11. Frequency spectra of C_L for (a) flow past a diamond cylinder at Re = 180, and (b) flow past a circular cylinder at Re = 250.

Fig. 12 shows the *St*–*Re* relationship over the wake transition regimes for flow past a diamond cylinder. At the onset of three-dimensionality, a sudden drop in the *St* value (of 5.6%) is observed, which, according to Jiang et al. (2018a), is consistent with the subcritical nature of the mode A instability for a diamond cylinder (Sheard et al., 2009) and the associated sudden increase in the degree of flow three-dimensionality at Re_{cr} (Fig. 8b). For $Re > Re_{cr}$, a continuous *St*–*Re* relationship is observed for the 3D flows, including the mode swapping regime highlighted in Fig. 12, since the twin-peaked pattern is not observed for the frequency spectra shown in Fig. 10.

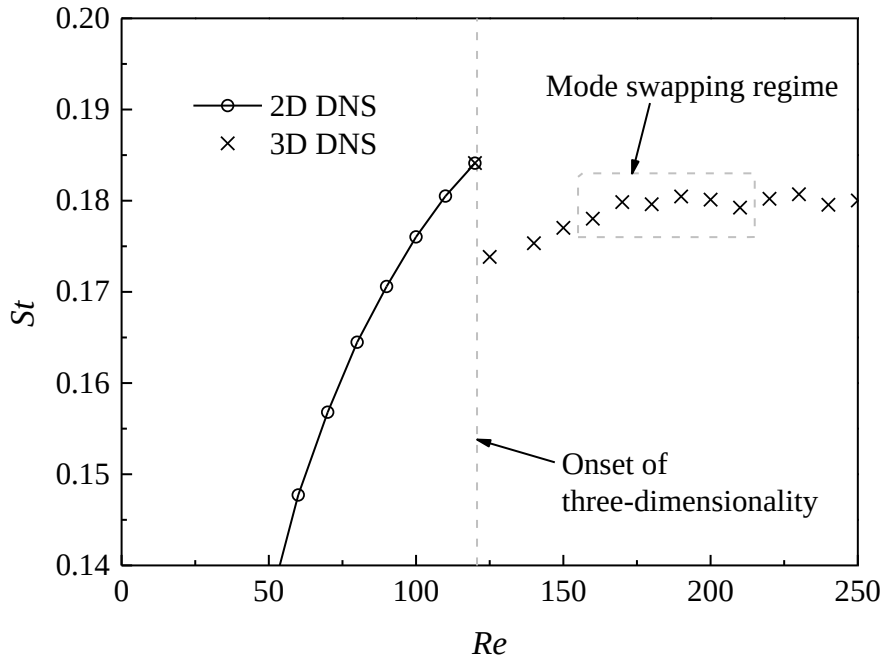

Fig. 12. The *St*–*Re* relationship over the wake transition regimes.

3.4. The drag coefficient

Fig. 13 shows the $\overline{C_D} - Re$ relationship over the wake transition regimes. In addition, the total drag coefficient is decomposed into the pressure and viscous components. The present 2D results agree relatively well with those reported by Yoon et al. (2010). As *Re* exceeds the onset of the primary wake instability, the pressure drag starts to increase while the viscous drag continues to decrease, which is similar to that of a circular cylinder investigated in Henderson (1995). However, a difference to a circular cylinder (Henderson, 1995) or a square cylinder (Jiang and Cheng, 2018) is that for a diamond cylinder the increase rate of the pressure drag is larger than the decrease rate of the viscous drag, such that the total drag exhibits an increase right after the onset of the primary wake instability. At the onset of the secondary wake instability, both the pressure and viscous drag display an approximately 7% decrease, which is consistent with the sudden decrease/increase in *St* (Fig. 12), C_L' (Fig. 8a) and the degree of flow three-dimensionality (Fig. 8b) discussed in sections 3.2 and 3.3.

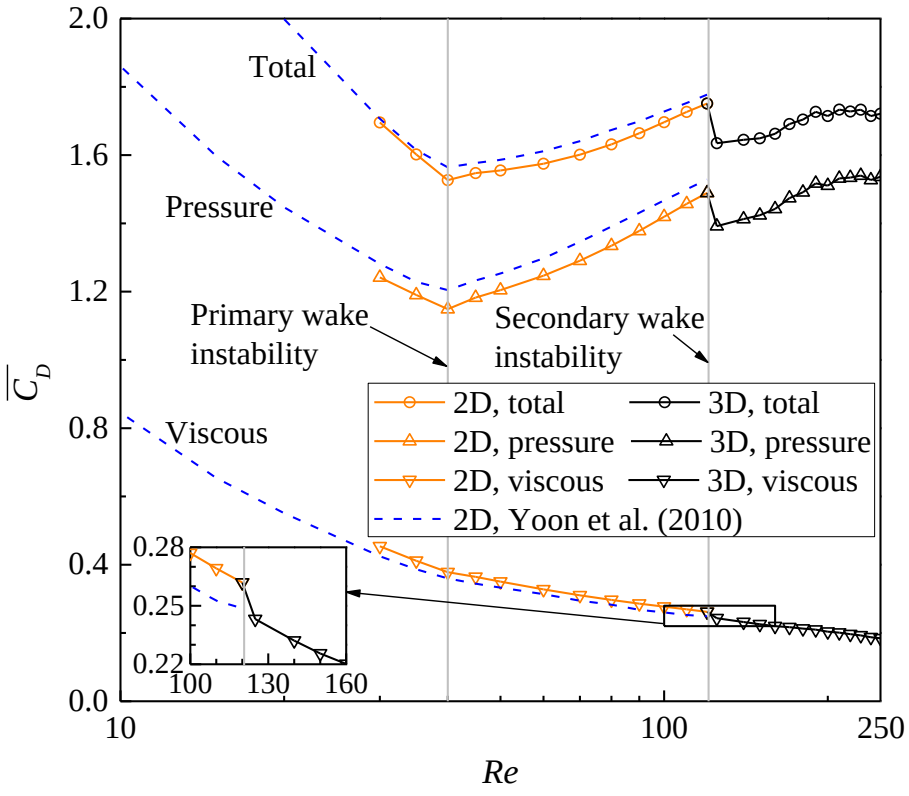

Fig. 13. The $\overline{C_D} - Re$ relationship over the wake transition regimes.

Based on the decomposition of the pressure and viscous drag coefficients (denoted $\overline{C_{D,p}}$ and $\overline{C_{D,v}}$, respectively) in Fig. 13, the ratio between the pressure

drag and the total drag ($\overline{C_{D,p}}/\overline{C_D}$) is quantified in Fig. 14. In comparison, Fig. 14 also shows the results for a circular cylinder, a square cylinder (with α = 0°) and inclined square cylinders with α = 15.3° and 29.7°, based on the $\overline{C_{D,p}}$ and $\overline{C_{D,v}}$ values reported by Jiang and Cheng (2018) and Yoon et al. (2010). The red vertical bars in Fig. 14 indicate the onset of three-dimensionality for circular, square and diamond cylinders, where the 3D results appear to the right of them. In addition, the 2D simulations have been extended beyond the onset of three-dimensionality (although unphysical in real situations), and the 2D results show excellent agreement with the corresponding 3D results. The agreement between the 2D and 3D results is attributed to a very similar percentage decrease in the pressure and viscous drag at the onset of three-dimensionality (e.g. Fig. 13). Therefore, the 2D results for α = 15.3° and 29.7° can be used without having to consider the effect of three-dimensionality.

A common feature for the cylinders investigated in Fig. 14 is that for each cross-sectional shape the projected length perpendicular to the incoming flow (which contributes to the pressure drag) is the same as the projected length parallel to the incoming flow (which contributes to the viscous drag). Therefore, the ratio $\overline{C_{D,p}}/\left(\overline{C_{D,p}}+\overline{C_{D,v}}\right)=\overline{C_{D,p}}/\overline{C_D}$ serves as a direct indication of the bluffness of the cylinder. As shown in Fig. 14, the $\overline{C_{D,p}}/\overline{C_D}$ value, and hence the bluffness of the cylinder, is largest for a square cylinder, followed by inclined square cylinders with increasing α from 0° to 45°, and smallest for a circular cylinder.

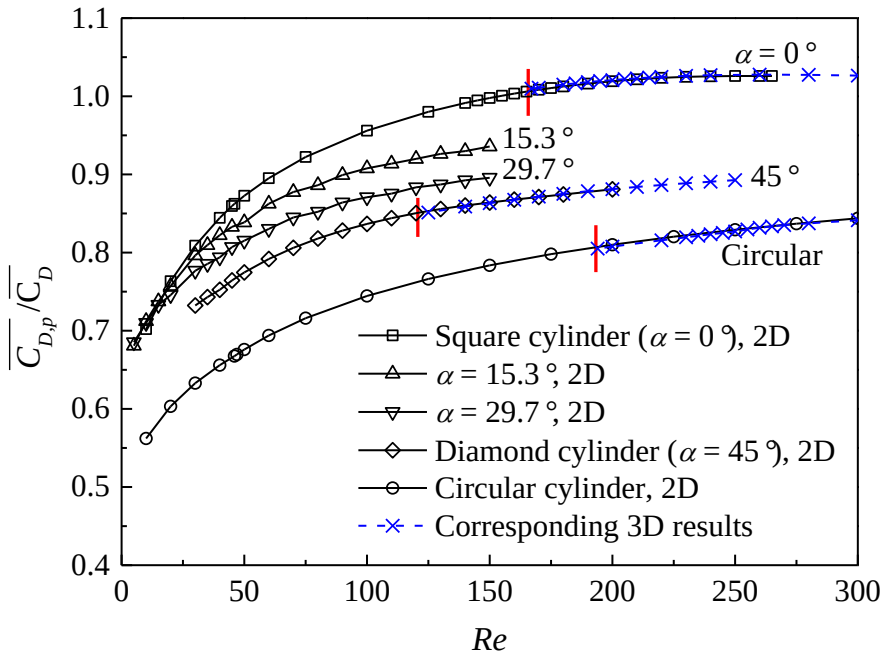

Fig. 14. The ratio between the pressure drag and the total drag for different cylinders. The red vertical bars indicate the onset of three-dimensionality.

3.5. Floquet analysis of the 3D wake instability modes

As discussed in section 3.1, the mode B structures observed at $Re \geq 150$ are destabilised by the mode A structures that exist in the wake. On the other hand, it is also of interest to examine the global instability of mode B (and other modes) to the 2D base flow, where the interactions between the modes A and B structures are eliminated. In general, Floquet stability analysis has been a preferred method in determining the 3D modes that are unstable to the 2D base flow, e.g. the mode B instability of a circular cylinder (Barkley and Henderson, 1996; Posdziech and Grundmann, 2001) and a square cylinder (Robichaux et al., 1999; Sheard et al., 2009; Park and Yang, 2016), among many others. A necessary condition for the use of the Floquet analysis is that the 2D base flow is time-periodic (Barkley and Henderson, 1996). For a diamond cylinder, however, Sheard et al. (2009) found that the 2D base flow became aperiodic at $Re \gtrsim 140$, such that no Floquet analysis had been performed for $Re \gtrsim 140$ to identify the instability modes other than mode A.

In the present study, the 3D instability modes of a diamond cylinder for $Re \gtrsim 140$ are examined by the Floquet analysis with caution. The aperiodicity of the 2D base flow is illustrated in Fig. 15(a,b) at $Re = 300$ with two instantaneous vorticity fields of one primary vortex shedding period ($T^* = TU/h$) apart, where the vorticity fields become aperiodic at $x/h \gtrsim 7$. In addition, Fig. 15(c) shows the locations of the vortex centres extracted from 19 snapshots of the vorticity field (including the vorticity field shown in Fig. 15(a)), which illustrates more clearly that the wake becomes aperiodic at $x/h \gtrsim 7$. The two vertical dashed lines in each panel of Fig. 15 mark the streamwise locations where the wake transitions from the primary vortex street to the two-layered and the secondary vortex streets. The transition locations are determined as the x/h values corresponding to the local maxima in the time-averaged transverse velocity field shown in Fig. 15(d) (Jiang and Cheng, 2019). A mesh convergence check conducted at $Re = 300$ (the largest Re considered by the Nektar++ model used in this section) shows that an increase in N_p from 5 to 7 results in variations in the two transition locations of 0.5%, which suggests that the use of $N_p = 5$ is adequate. As shown in Fig. 15(a–c), the wake remains periodic when the primary vortices rearrange themselves to the two-layered pattern, while the wake gradually becomes aperiodic when the two-layered vortices rearrange themselves for the irregular vortex merging (see e.g. Fig. 15b) at the transition to the secondary vortex street. In other words, the aperiodicity of the 2D base flow arises from the transition from the two-layered to the secondary vortex street. Such a transition is not observed for $Re = 140$ within the wake domain length up to $x/h = 40$ (and the entire wake is perfectly periodic), but is observed for $Re \geq 160$ (and the wake is aperiodic), such that the Floquet analysis of $Re \geq 160$ should be conducted with caution.

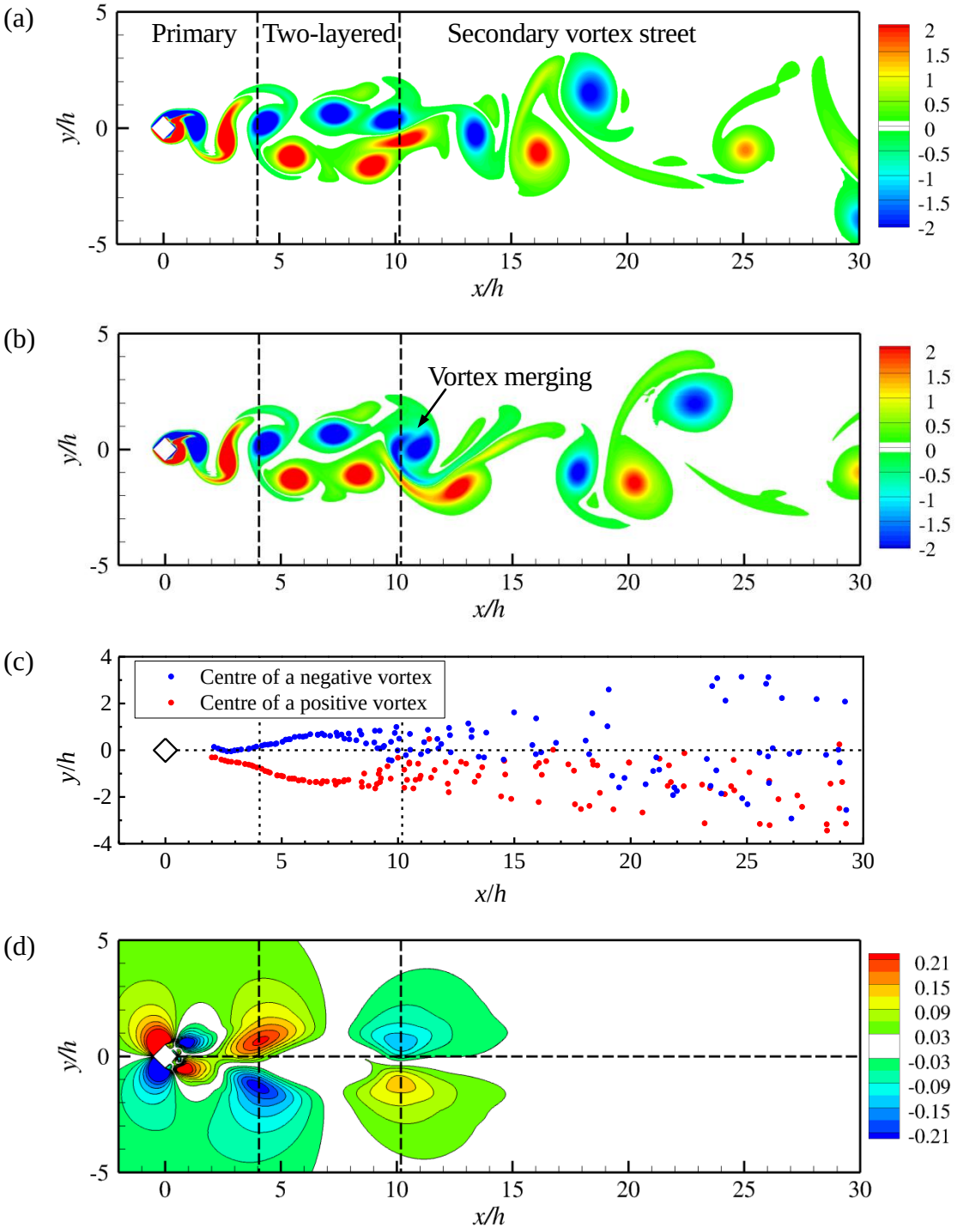

Fig. 15. Characteristics of the 2D base flow for Re = 300: (a) instantaneous vorticity field at t^* = 1400, (b) instantaneous vorticity field at t^* = 1400 + T^*, (c) locations of the vortex centres extracted from 19 snapshots of the vorticity field (at t^* = 1000 to 2800 with an interval of 100), and (d) time-averaged transverse velocity field. The vertical dashed lines mark the two transition locations, while the horizontal dashed line in panels (c) and (d) marks the wake centreline.

Fig. 16 shows the $|\mu|$–β relationships for Re = 300, predicted through the Floquet analysis using two different vortex shedding periods of base flows, i.e. t^* = 1400 –

(1400 + T*) and t* = 1600 – (1600 + T*). It is found that the aperiodicity of the base flow results in quantitative uncertainties in the $|\mu|$–β relationship, while qualitatively the unstable peaks (i.e. the wake instability modes) are the same. The first peak at βh ~ 0.8 – 1.8 contains real and positive μ values, which correspond to the mode A instability. The second peak at βh ~ 2.8 – 4 contains real and negative μ values, which correspond to a subharmonic mode. Based on further computations, the critical Re for the instability of the subharmonic mode is located within 280 – 285. Other than these two modes, no additional instability modes are identified by the Floquet analysis over Re = 120 – 300 (with an interval of 20).

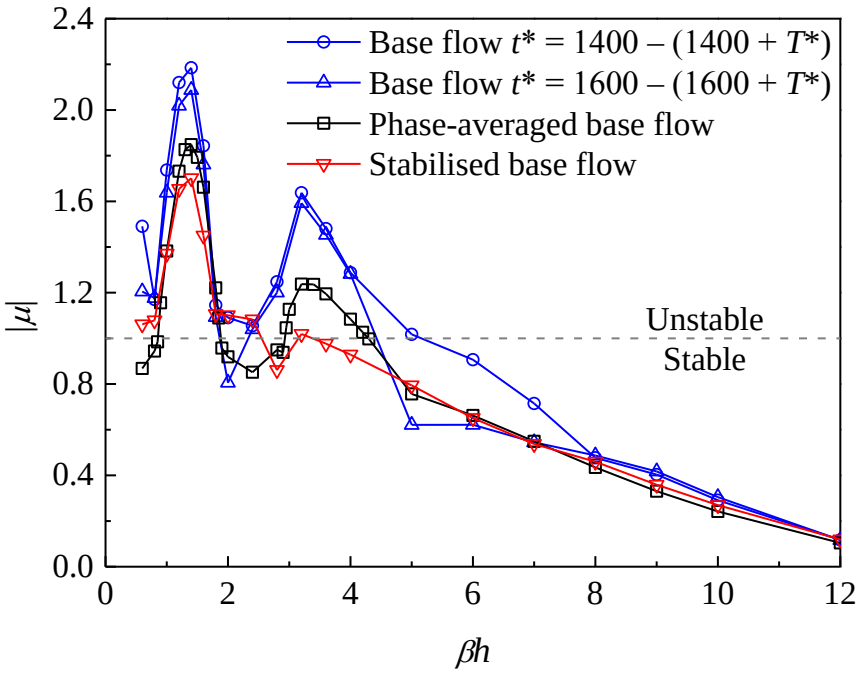

Fig. 16. The $|\mu|$–β relationships for Re = 300, predicted through the Floquet analysis using different base flows. The horizontal dashed line marks the neutral instability of $|\mu|$ = 1.0.

To eliminate the quantitative uncertainties in the $|\mu|$–β relationship induced by the aperiodicity of the base flow, phase-averaged (hence T-periodic) base flow is attempted for the Floquet analysis. The phase-averaged base flow is generated based on 200T of the fully developed original 2D flow. Fig. 17(a,b) illustrates the phase-averaged base flow for Re = 300 at two phases of T/2 apart. The $|\mu|$–β relationship predicted using the phase-averaged base flow is also shown in Fig. 16, where, similarly, a mode A and a subharmonic mode are obtained, which suggests again that the aperiodicity of the base flow induces quantitative but not qualitative influence on the Floquet instability modes. Based on the phase-averaged base flow, Floquet analyses were performed for $Re \geq 160$. Fig. 18 shows the extended neutral instability curve for mode A up to Re = 300 (cf. Fig. 3b). In addition, the subharmonic instability mode is identified at $Re \geq 285$.

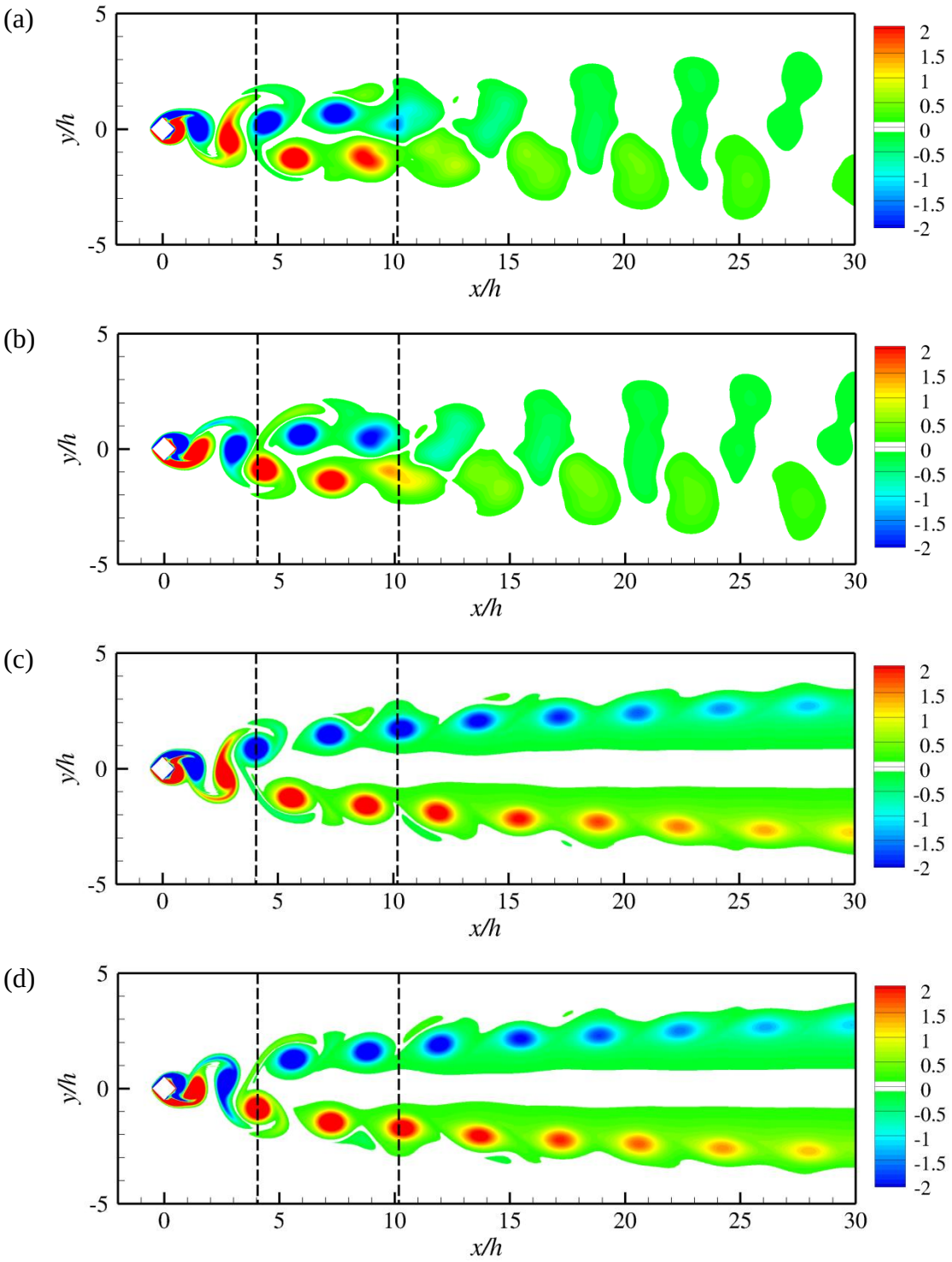

Fig. 17. Illustration of T-periodic base flows for Re = 300. Panels (a) and (b) show instantaneous vorticity fields for the phase-averaged base flow at two phases of $T/2$ apart, while panels (c) and (d) show instantaneous vorticity fields for the stabilised base flow at two phases of $T/2$ apart. The base flows in panels (a) and (c) are shown at the same phase as Fig. 15(a,b). The vertical dashed lines mark the two transition locations for the original aperiodic 2D flow.

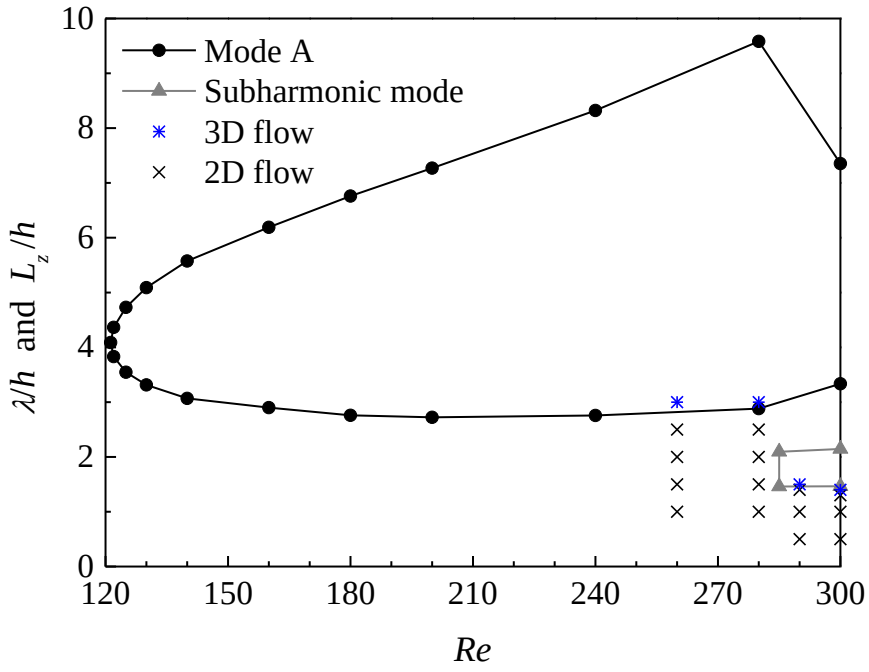

Fig. 18. The neutral instability curves for mode A and the subharmonic mode. The Floquet analyses for $Re \geq 160$ are performed based on the phase-averaged base flow.

To further confirm the existence of the subharmonic instability mode predicted by the Floquet analysis, 3D DNS were conducted using L_z/h = 1 – 3 to eliminate the influence of mode A and to reveal the relatively small-scale subharmonic instability mode. The present DNS cases and their 2D or 3D near-wake patterns are summarised in Fig. 18 using isolated symbols. The DNS results agree well with the neutral instability curves. For Re = 260 and 280, the near wake becomes 3D when L_z/h increases from 2.5 to 3, and the wake of L_z/h = 3 is represented by one spanwise period of the mode A structure. For Re = 290, the near wake first becomes 3D when L_z/h increases from 1.4 to 1.5, and the near wake is represented by one spanwise period of the subharmonic mode. The subharmonic mode observed at L_z/h = 1.5 is free from the influence of mode A that may appear at larger L_z/h values. The existence of the subharmonic instability mode is thus cross-checked by both DNS and the Floquet analysis, where both methods predict its onset of instability at Re within 280 – 290.

The subharmonic mode is also observed at Re = 300 when L_z/h increases from 1.3 to 1.4. The subharmonic mode at Re = 300 and L_z/h = 1.4 is investigated in detail by examining the instantaneous ω_z and ω_x fields over a period of 20T. Fig. 19 illustrates the ω_z (the left column) and ω_x (the right column) fields at the plane z/h = 0.1 over a period of 2T. The top row of Fig. 19 is shown at an arbitrary time instant in the fully developed flow, while the middle and bottom rows are shown at time evolutions of T and 2T, respectively. It is seen that the ω_z fields shown in Fig. 19(a,c,e) are generally T-periodic at $x/h \lesssim 7$, which is similar to those of the 2D flow shown in Fig. 15(a,b). However, while the $|\omega_x|$ fields in Fig. 19(b,d,f) are generally T-periodic at $x/h \lesssim 7$, the streamwise vortices change sign every T, resulting in the period-doubling of the flow.

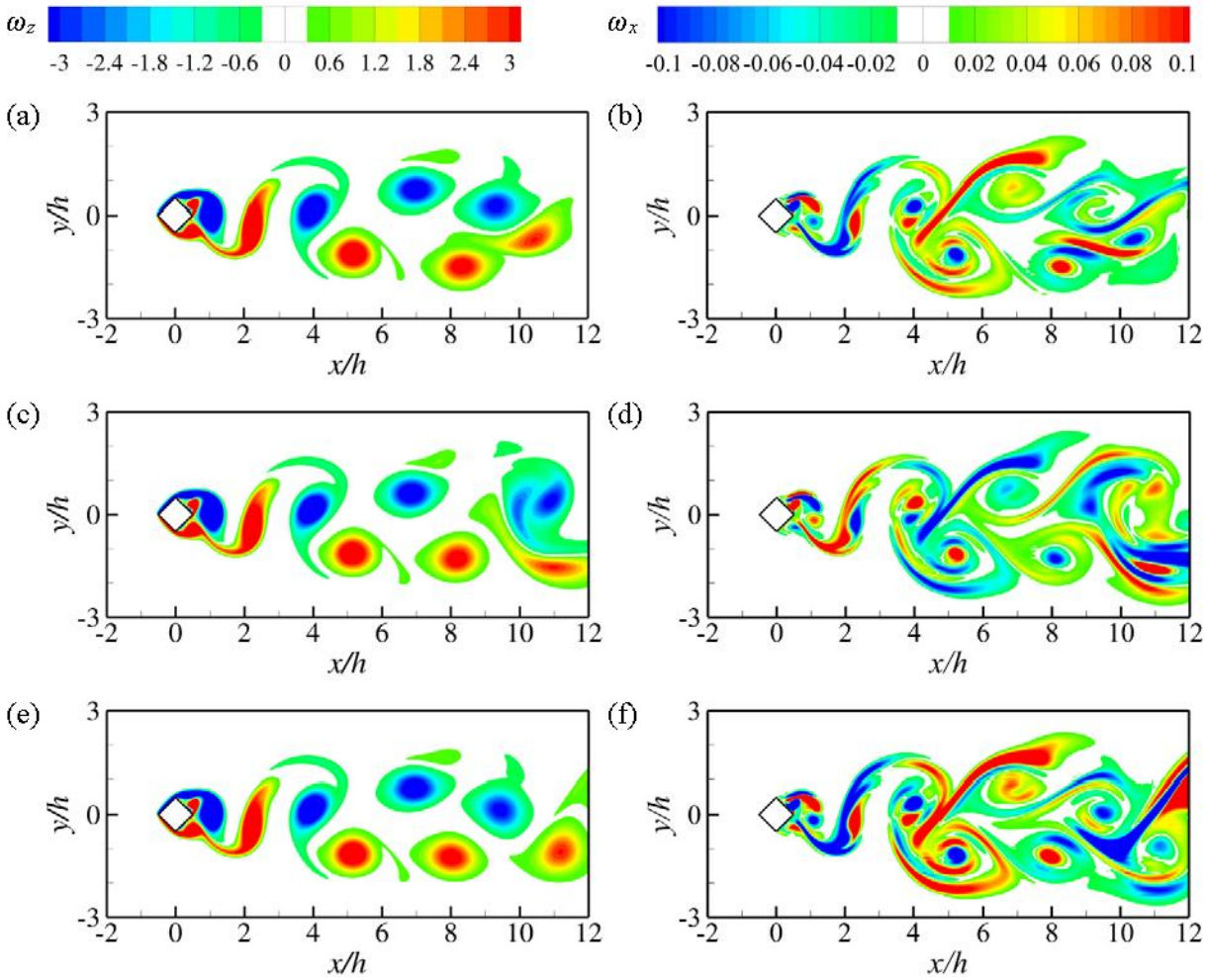

Fig. 19. Instantaneous ω_z (the left column) and ω_x (the right column) fields at the plane z/h = 0.1 for the 3D DNS case of Re = 300 and L_z/h = 1.4. The top row is shown at an arbitrary time instant in the fully developed flow, while the middle and bottom rows are shown at time evolutions of T and 2T, respectively.

The physical mechanism for the development of the subharmonic mode is investigated below. It is anticipated that the development of the subharmonic mode is related to the development of the secondary vortex street relatively close to the cylinder. To prove this point, additional Floquet analysis was conducted by using a base flow without the transition to the secondary vortex street. The transition to the secondary vortex street can be suppressed by stabilising the two-layered vortex street till the outlet boundary (see Fig. 17c,d) through the following procedures:

(i) Compute the fully developed 2D flow and the corresponding vortex shedding period T.

(ii) Repeat the following until the two-layered vortex street is stabilised till the outlet: advance the flow by a period of T, and use the average of the flow fields at the beginning and the end of the T-period as the initial condition for the next iteration.

(iii) Compute the updated T for the stabilised flow field.

(iv) Repeat steps (ii) and (iii) until the updated T does not change.

It is worth noting that the stabilised base flow is strictly T-periodic, since the aperiodic transition to the secondary vortex street is suppressed.

Based on the stabilised base flow, the $|\mu|$–β relationship for Re = 300 is also shown in Fig. 16. While the first peak at $\beta h \sim 0.8 – 1.8$ still corresponds to the mode A instability, the second peak, which is marginally unstable at $\beta h = 3.2$ with a real and positive μ value (rather than a real and negative μ for the subharmonic mode), corresponds to a wake instability in the two-layered vortex street near the outlet, which would not exist in the original base flow.

The disappearance of the subharmonic mode in the stabilised base flow sheds light on the origin of the subharmonic mode. For the original base flow (and naturally also the phase-averaged base flow), it is found that the time-averaged flow becomes asymmetric about the wake centreline at $Re \geq 285$ (e.g. Fig. 15d). Consistently, the time-averaged lift coefficient becomes non-zero, the trajectories for the positive and negative vortices become asymmetric about the wake centreline (Fig. 15c), and the corresponding phase-averaged base flow (Fig. 17a,b) breaks the following spatiotemporal symmetry

$$\omega_z(x, y, t) = -\omega_z(x, -y, t + T/2), \tag{3.5}$$

Physically, subharmonic modes are often detected by the Floquet analysis when the base flow breaks the above spatiotemporal symmetry (Blackburn and Sheard, 2010), even when the bluff body and the incoming flow are symmetric about the wake centreline (e.g. Serson et al., 2014). Therefore, it is not surprising that the critical Re for the asymmetry of the time-averaged flow coincides with the critical Re for the instability of the subharmonic mode (both at Re = 280 – 285). In contrast, the stabilised base flow (Fig. 17c,d) possesses the spatiotemporal symmetry given in equation (3.5), such that no subharmonic mode is detected by the Floquet analysis. A comparison between the original/phase-averaged base flow and the stabilised base flow suggests that the breaking of the spatiotemporal symmetry described in equation (3.5) is induced by the transition to the secondary vortex street relatively close to the cylinder, which rearranges the near-wake vortex pattern upstream of the transition.

Although the subharmonic mode is detected by the Floquet analysis and 3D DNS with L_z smaller than the spanwise wavelengths of mode A at $Re \gtrsim 285$, it may not exist in the natural 3D flow. Instead, section 3.1 shows that the mode B structures are observed in the natural 3D flow at $Re \geq 150$ and dominate the wake at $Re \geq 220$, although none of the Floquet analysis conducted here detects the mode B instability. In addition, Table 2 summarises the wake structures for Re = 300 predicted by the 3D DNS under different L_z/h constraints. A mesh convergence check was performed for the case L_z/h = 12 by increasing N_p from 5 to 6, where the St, $\overline{C_D}$ and C_L' values vary by less than 1%. It is seen in Table 2 that with increasing L_z/h from 3 to 6, the wake structure changes from the ordered subharmonic mode (Fig. 20a) to disordered mode B (Fig. 20b). The existence of mode B rather than the subharmonic mode for L_z/h = 6 and 12 is supported by the following evidence.

(i) The streamwise vortices possess the spatiotemporal symmetry corresponding to mode B rather than the subharmonic mode.

(ii) The time-averaged lift coefficient is practically zero (of the order of 10^{-4}).

(iii) The mode B structures emerge at $Re \geq 150$, which is much smaller than the onset of the subharmonic mode at $Re \sim 285$.

Table 2. Wake structures for Re = 300 predicted by the 3D DNS under different L_z/h constraints.

L_z/h	Streamwise vortices	Spanwise vortices	$\lvert\overline{C_L}\rvert$
0	n/a	Ordered	0.037
1.4	One spanwise period of the ordered subharmonic mode	Ordered	0.032
1.5	One spanwise period of the ordered subharmonic mode	Ordered	0.029
3	Two spanwise periods of the ordered subharmonic mode (Fig. 20a)	Ordered (Fig. 20a)	0.029
6	Disordered mode B (Fig. 20b)	Disordered (Fig. 20b)	O(10^{-4})
12	Disordered mode B	Disordered	O(10^{-4})

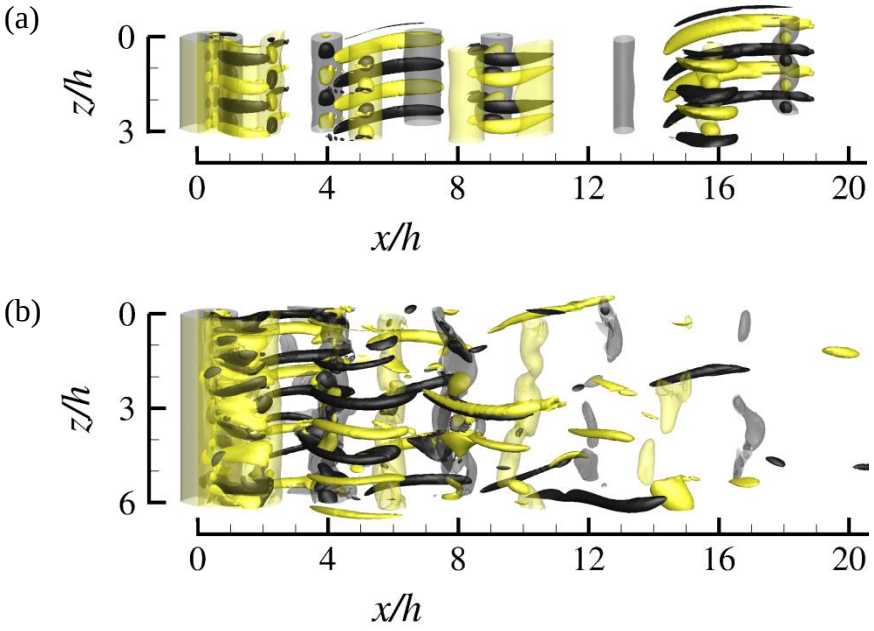

Fig. 20. Instantaneous vorticity fields for Re = 300 predicted by the 3D DNS using (a) L_z/h = 3 and (b) L_z/h = 6. The translucent iso-surfaces represent spanwise vortices with $\omega_z = \pm 2$, while the opaque iso-surfaces represent streamwise vortices with $\omega_x = \pm 0.4$ for panel (a) and $\omega_x = \pm 2$ for panel (b). Dark grey and light yellow denote positive and negative vorticity values, respectively. The flow is from left to right past the cylinder on the left.

The development of mode B rather than the subharmonic mode in the natural 3D

flow is attributed to the influence of the mode A instability. The mode A streamwise vortices may destabilise mode B through (i) destabilising the braid shear layer region (Jiang et al., 2016) for the hyperbolic instability of mode B (Williamson, 1996; Leweke and Williamson, 1998; Thompson et al., 2001), and (ii) modulating the pattern of the spanwise vortices (i.e. the base flow) to allow for the instability of mode B. To demonstrate the latter mechanism, the span-averaged spanwise vorticity fields for Re = 300 computed with L_z/h = 3 and 6 are shown in Fig. 21. For L_z/h = 3, the ordered streamwise vortices of the subharmonic mode do not induce noticeable influence on the spanwise vortices (Fig. 20a), such that the pattern of the spanwise vortices shown in Fig. 21(a) is similar to that computed with 2D DNS (Fig. 15a,b), where the primary vortex street transitions to the two-layered and secondary vortex streets at x/h ~ 4 and 10, respectively. For L_z/h = 6, the spanwise vortices are highly disordered (Fig. 20b), such that the spanwise vorticity field shown in Fig. 21(b) is based on a phase average over 25 vortex shedding cycles. Compared with Fig. 21(a), the pattern and strength of the spanwise vortices shown in Fig. 21(b) are significantly modulated by the disordered streamwise vortices (Fig. 20b) and the associated development of turbulence and turbulent dissipation.

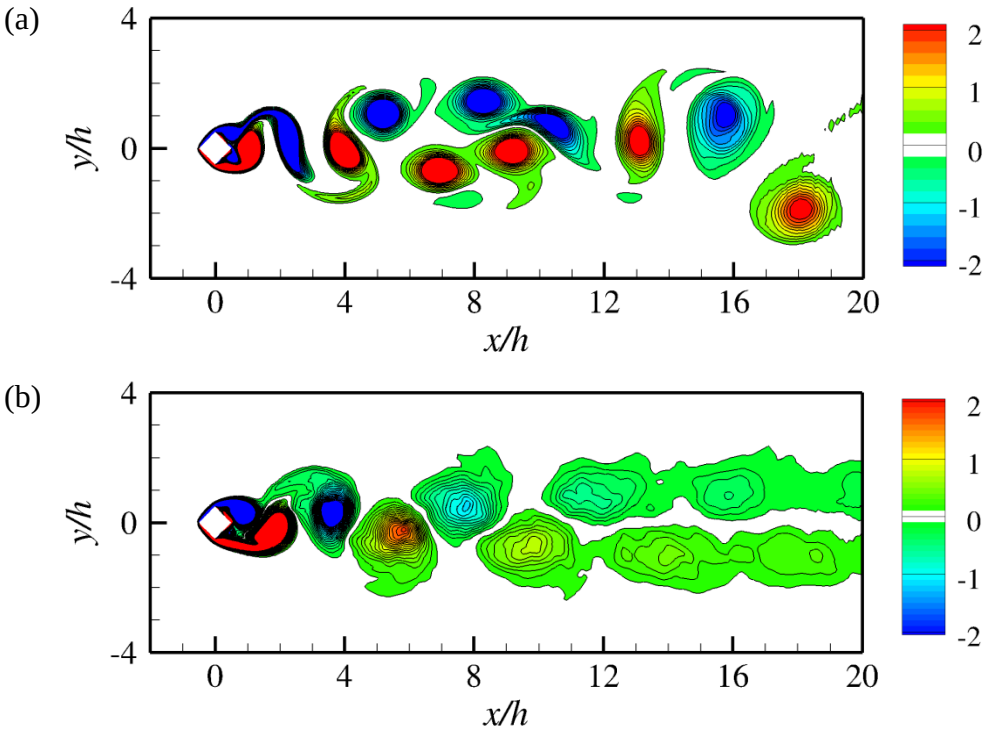

Fig. 21. Span-averaged spanwise vorticity fields for Re = 300, obtained from (a) the instantaneous 3D flow field shown in Fig. 20(a) computed with L_z/h = 3, and (b) the phase-averaged 3D flow computed with L_z/h = 6.

It is anticipated that the modulated pattern of the spanwise vortices may give rise to the instability of mode B. Therefore, an additional Floquet analysis is conducted, where the base flow is the phase- and span-averaged spanwise vorticity fields for Re = 300 obtained with L_z/h = 6 (called the modulated base flow hereafter). Fig. 22 shows

the $|\mu|$–β relationship for Re = 300, predicted through the Floquet analysis using the modulated base flow. The two unstable modes identified in Fig. 22 both contain real and positive μ values, which correspond to synchronous modes. The streamwise perturbation vorticity fields for the two modes are shown in Fig. 23(a,b). The perturbation patterns of the two modes agree well with those for modes A and B for circular and square cylinders (see e.g. Carmo et al., 2010; Robichaux et al., 1999). The most unstable spanwise wavelength for mode B (~ 0.9h) is similar to the wavelengths for mode B for circular and square cylinders (Barkley and Henderson, 1996; Choi et al., 2012; Park and Yang, 2016).

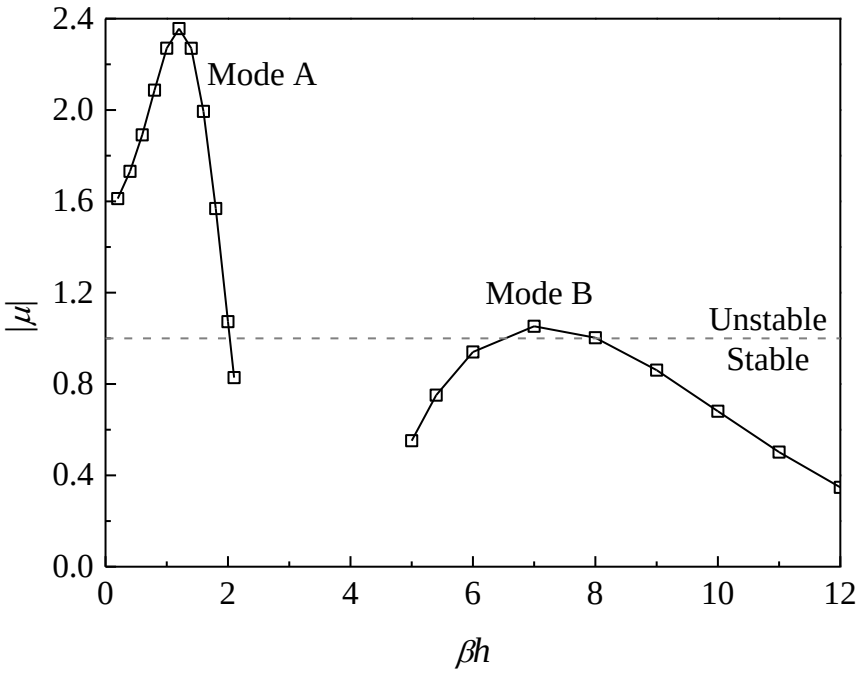

Fig. 22. The $|\mu|$–β relationship for Re = 300, predicted through the Floquet analysis using the modulated base flow. The horizontal dashed line marks the neutral instability of $|\mu|$ = 1.0.

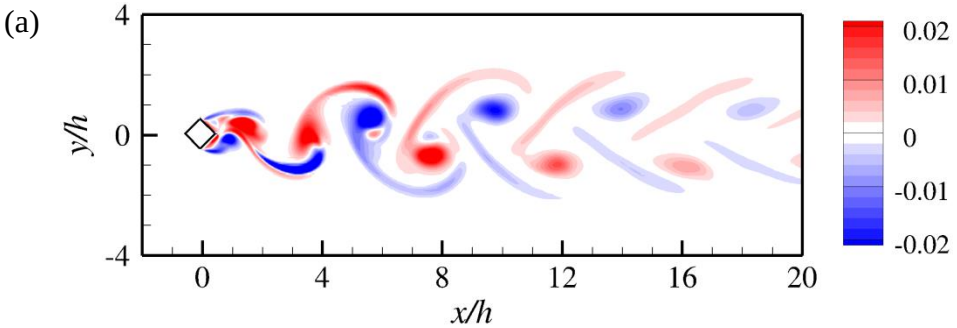

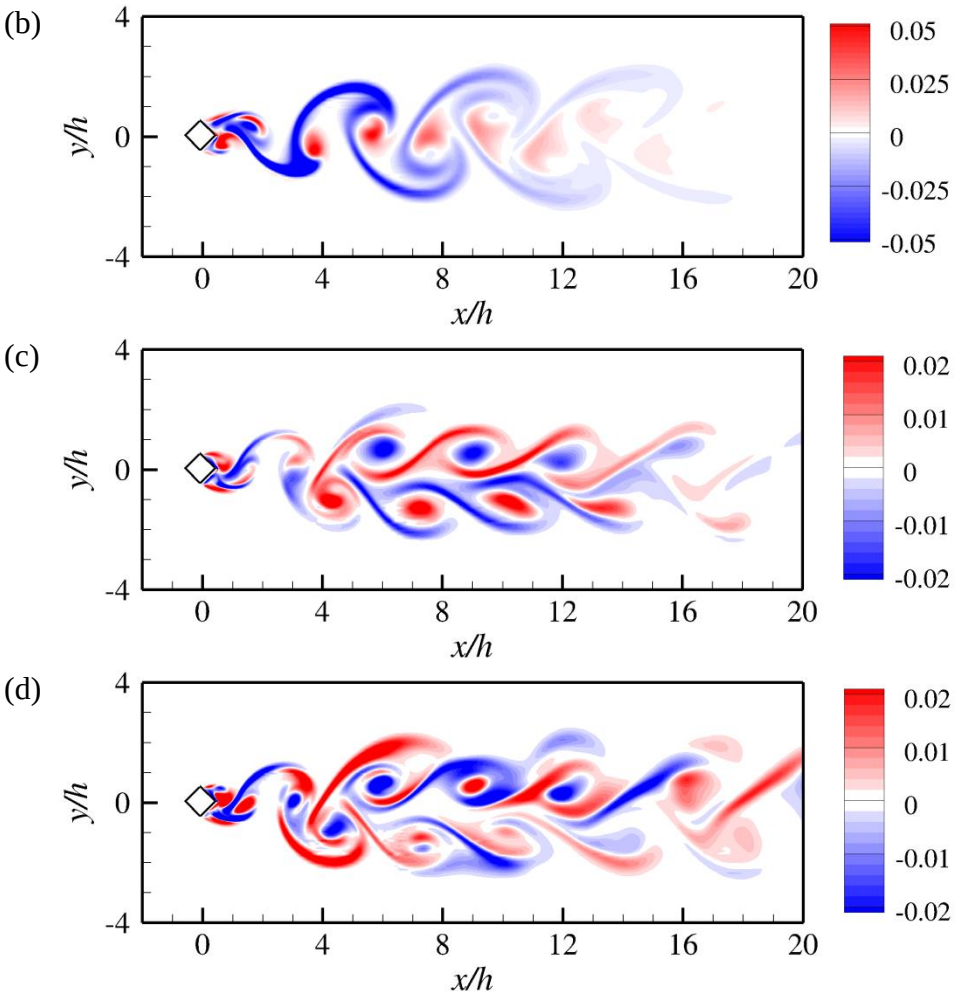

Fig. 23. Streamwise perturbation vorticity fields for Re = 300: (a) mode A predicted by βh = 1.8 of the modulated base flow, (b) mode B predicted by βh = 7 of the modulated base flow, (c) mode A predicted by βh = 1.4 of the phase-averaged base flow, and (d) the subharmonic mode predicted by βh = 3.2 of the phase-averaged base flow. Red and blue denote positive and negative vorticity values, respectively.

For completeness, Fig. 23(c,d) shows the streamwise perturbation vorticity fields for mode A and the subharmonic mode predicted with the phase-averaged base flow illustrated in Fig. 17(a,b). For mode A, the perturbation structure displays opposite signs for the two sides of the wake centreline (Fig. 23a,c). For the subharmonic mode, the perturbation structure displays both signs alternately at each side of the wake centreline (Fig. 23d). The most unstable spanwise wavelength for the subharmonic mode (~ 1.9h) is similar to the wavelengths for the subharmonic mode observed in the wake of other bluff bodies (e.g. Sheard et al., 2009; Yildirim et al., 2013).

However, Fig. 22 shows that the subharmonic mode is suppressed by the modulated pattern of the spanwise vortices shown in Fig. 21(b). As discussed earlier in this section, the subharmonic mode is unstable to the original and phase-averaged base flows where the spatiotemporal symmetry described in equation (3.5) is broken by the transition to the secondary vortex street relatively close to the cylinder. For the modulated base flow shown in Fig. 21(b), the two-layered vortices with significantly

weakened vorticity do not transition to the secondary vortex street, and the wake possesses the spatiotemporal symmetry (see e.g. the $\left|\overline{C_L}\right|$ values in Table 2), such that the subharmonic mode is suppressed.

4. Conclusions

This paper investigates numerically the 3D wake transition process of a diamond cylinder. Detailed 3D DNS show that the wake becomes 3D at Re_{cr} ~ 121 and is represented by mode A with global vortex dislocations for $Re = Re_{cr} - 150$. For Re = 160 – 210, a mode swapping between modes A and B takes place. With the increase in Re, the mode B structures are increasingly likely destabilised by the streamwise vortices of mode A, and consequently the probability of occurrence of mode A with global vortex dislocations decreases monotonically. For $Re \geq 220$, the wake is dominated by increasingly disordered mode B structures.

For the mode swapping regime, the different characteristics of the dislocation and non-dislocation periods are analysed quantitatively through a new approach. Specifically, a specific flow property (e.g. C_L', ε_x, ε_y, St, etc.) can be decomposed into the values corresponding to the dislocation and non-dislocation time periods. Owing to the vortex dislocations, the C_L' and St values for the dislocation periods are smaller than their counterparts for the non-dislocation periods, and consistently the ε_x and ε_y values (i.e. the degree of flow three-dimensionality) show the opposite. Quantitatively, the C_L', ε_x, ε_y and St values for the non-dislocation periods are closer to those for the dislocation branch than their 2D counterparts. Therefore, the overall C_L'–Re, ε_x–Re and ε_y–Re curves, which are bounded by the dislocation and non-dislocation branches, display only slight changes in the variation trends when the overall curve detaches the dislocation branch at Re ~ 160 and attaches the non-dislocation branch at Re ~ 210. In addition, the relatively close St values for the dislocation and non-dislocation periods cannot be distinguished as two peaks in the overall frequency spectrum.

In contrast, a similar analysis for the circular cylinder case shows that the non-dislocation branch is much closer to the 2D curve than the dislocation branch, such that the overall curve displays an obvious peak/trough towards its 2D counterpart at the upper end of the mode swapping regime, commonly known as a critical condition (Williamson, 1996). In addition, the St values for the dislocation and non-dislocation periods are now sufficiently apart to be distinguished as two peaks in the overall frequency spectrum.

In addition to DNS, Floquet stability analyses are conducted to identify the 3D wake instability modes of a diamond cylinder up to Re = 300. Phase-averaged base flow is adopted to eliminate the quantitative uncertainties induced by the aperiodic secondary vortex street in the base flow. In addition to mode A, a subharmonic instability mode is identified at $Re \geq 285$, whereas mode B is not detected. The subharmonic instability mode is induced by the breaking of the Z_2 spatiotemporal symmetry of the base flow, which is further induced by the transition to the secondary vortex street relatively close to the cylinder and rearrangement of the near-wake

vortex pattern upstream of the transition.

The disagreement between the natural 3D flow and the Floquet analysis regarding the existence of mode B and the subharmonic mode is explained. For the natural 3D flow, the existence of mode A modulates the pattern of the spanwise vortices (i.e. the base flow), which gives rise to the instability of mode B. In addition, the base flow modulated by the existence of modes A and B does not transition to the secondary vortex street, which suppresses the subharmonic mode. In summary, the natural 3D flow involves complex interactions between the streamwise and spanwise vortices, as well as between the 3D wake transition and the 2D base-flow transition.

Acknowledgments

The author would like to acknowledge the support from the Australian Research Council through the DECRA scheme (Grant No. DE190100870). This work was supported by resources provided by the Pawsey Supercomputing Centre with funding from the Australian Government and the Government of Western Australia.

Declaration of interests

The author reports no conflict of interest.

References

Akbar, T., Bouchet, G., Dušek, J., 2011. Numerical investigation of the subcritical effects at the onset of three-dimensionality in the circular cylinder wake. Physics of Fluids 23, 094103.

Barkley, D., Henderson, R.D., 1996. Three-dimensional Floquet stability analysis of the wake of a circular cylinder. Journal of Fluid Mechanics 322, 215–241.

Barkley, D., Tuckerman, L.S., Golubitsky, M., 2000. Bifurcation theory for three-dimensional flow in the wake of a circular cylinder. Physical Review E 61, 5247–5252.

Blackburn, H.M., Lopez, J.M., 2003. On three-dimensional quasiperiodic Floquet instabilities of two-dimensional bluff body wakes. Physics of Fluids 15, L57–L60.

Blackburn, H.M., Sheard, G.J., 2010. On quasiperiodic and subharmonic Floquet wake instabilities. Physics of Fluids 22, 031701.

Cantwell, C.D., et al., 2015. Nektar++: An open-source spectral/hp element framework. Computer Physics Communications 192, 205–219.

Carmo, B.S., Meneghini, J.R., Sherwin, S.J., 2010. Secondary instabilities in the flow around two circular cylinders in tandem. Journal of Fluid Mechanics 644, 395–431.

Choi, C., Jang, Y., Yang, K., 2012. Secondary instability in the near-wake past two tandem square cylinders. Physics of Fluids 24, 024102.

Henderson, R.D., 1995. Details of the drag curve near the onset of vortex shedding. Physics of Fluids 7, 2102–2104.

Henderson, R.D., 1997. Nonlinear dynamics and pattern formation in turbulent wake transition. Journal of Fluid Mechanics 352, 65–112.

Henderson, R.D., Barkley, D., 1996. Secondary instability in the wake of a circular cylinder.

Physics of Fluids 8, 1683–1685.
Issa, R.I., 1986. Solution of implicitly discretized fluid flow equations by operator-splitting. Journal of Computational Physics 62, 40–65.
Jiang, H., Cheng, L., 2017. Strouhal–Reynolds number relationship for flow past a circular cylinder. Journal of Fluid Mechanics 832, 170–188.
Jiang, H., Cheng, L., 2018. Hydrodynamic characteristics of flow past a square cylinder at moderate Reynolds numbers. Physics of Fluids 30, 104107.
Jiang, H., Cheng, L., 2019. Transition to the secondary vortex street in the wake of a circular cylinder. Journal of Fluid Mechanics 867, 691–722.
Jiang, H., Cheng, L., An, H., 2017a. On numerical aspects of simulating flow past a circular cylinder. International Journal for Numerical Methods in Fluids, 85, 113–132.
Jiang, H., Cheng, L., An, H., 2018a. Three-dimensional wake transition of a square cylinder. Journal of Fluid Mechanics 842, 102–127.
Jiang, H., Cheng, L., An, H., Tong, F., Yang, F., 2018b. Flow past a diamond cylinder at moderate Reynolds numbers. 21st Australasian Fluid Mechanics Conference, Adelaide, Australia.
Jiang, H., Cheng, L., Draper, S., An, H., 2017b. Prediction of the secondary wake instability of a circular cylinder with direct numerical simulation. Computers & Fluids 149, 172–180.
Jiang, H., Cheng, L., Draper, S., An, H., Tong, F., 2016. Three-dimensional direct numerical simulation of wake transitions of a circular cylinder. Journal of Fluid Mechanics 801, 353–391.
Karniadakis, G.E., Sherwin, S.J., 2005. Spectral/hp Element Methods for CFD, *Oxford University Press*.
Leweke, T., Williamson, C.H.K., 1998. Three-dimensional instabilities in wake transition. European Journal of Mechanics - B/Fluids 17, 571–586.
Ng, Z.Y., Vo, T., Hussam, W.K., Sheard, G.J., 2016. Two-dimensional wake dynamics behind cylinders with triangular cross-section under incidence angle variation. Journal of Fluids and Structures 63, 302–324.
Park, D., Yang, K., 2016. Flow instabilities in the wake of a rounded square cylinder. Journal of Fluid Mechanics 793, 915–932.
Posdziech, O., Grundmann, R., 2001. Numerical simulation of the flow around an infinitely long circular cylinder in the transition regime. Theoretical and Computational Fluid Dynamics 15, 121–141.
Robichaux, J., Balachandar, S., Vanka, S.P., 1999. Three-dimensional Floquet instability of the wake of square cylinder. Physics of Fluids 11, 560–578.
Saha, A.K., 2007. Far-wake characteristics of two-dimensional flow past a normal flat plate. Physics of Fluids 19, 128110.
Serson, D., Meneghini, J.R., Carmo, B.S., Volpe, E.V., Gioria, R.S., 2014. Wake transition in the flow around a circular cylinder with a splitter plate. Journal of Fluid Mechanics 755, 582–602.
Sheard, G.J., Fitzgerald, M.J., Ryan, K., 2009. Cylinders with square cross-section: wake instabilities with incidence angle variation. Journal of Fluid Mechanics 630, 43–69.
Sheard, G.J., Thompson, M.C., Hourigan, K., 2003. A coupled Landau model describing the Strouhal–Reynolds number profile of a three-dimensional circular cylinder wake. Physics of Fluids 15, L68–L71.

Sohankar, A., Norberg, C., Davidson, L., 1999. Simulation of three-dimensional flow around a square cylinder at moderate Reynolds numbers. Physics of Fluids 11, 288–306.

Thompson, M.C., Leweke, T., Williamson, C.H.K., 2001. The physical mechanism of transition in bluff body wakes. Journal of Fluids and Structures 15, 607–616.

Thompson, M.C., Radi, A., Rao, A., Sheridan, J., Hourigan, K., 2014. Low-Reynolds-number wakes of elliptical cylinders: from the circular cylinder to the normal flat plate. Journal of Fluid Mechanics 751, 570–600.

Tong, X.H., Luo, S.C., Khoo, B.C., 2008. Transition phenomena in the wake of an inclined square cylinder. Journal of Fluids and Structures 24, 994–1005.

Williamson, C.H.K., 1996. Three-dimensional wake transition. Journal of Fluid Mechanics 328, 345–407.

Yildirim, I., Rindt, C.C.M., van Steenhoven, A.A., 2013. Energy contents and vortex dynamics in Mode-C transition of wired-cylinder wake. Physics of Fluids 25, 054103.

Yoon, D., Yang, K., Choi, C., 2010. Flow past a square cylinder with an angle of incidence. Physics of Fluids 22, 043603.

Yoon, D., Yang, K., Choi, C., 2012. Three-dimensional wake structures and aerodynamic coefficients for flow past an inclined square cylinder. Journal of Wind Engineering and Industrial Aerodynamics 101, 34–42.